



## 저작자표시-비영리-변경금지 2.0 대한민국

이용자는 아래의 조건을 따르는 경우에 한하여 자유롭게

- 이 저작물을 복제, 배포, 전송, 전시, 공연 및 방송할 수 있습니다.

다음과 같은 조건을 따라야 합니다:



저작자표시. 귀하는 원저작자를 표시하여야 합니다.



비영리. 귀하는 이 저작물을 영리 목적으로 이용할 수 없습니다.



변경금지. 귀하는 이 저작물을 개작, 변형 또는 가공할 수 없습니다.

- 귀하는, 이 저작물의 재이용이나 배포의 경우, 이 저작물에 적용된 이용허락조건을 명확하게 나타내어야 합니다.
- 저작권자로부터 별도의 허가를 받으면 이러한 조건들은 적용되지 않습니다.

저작권법에 따른 이용자의 권리는 위의 내용에 의하여 영향을 받지 않습니다.

이것은 [이용허락규약\(Legal Code\)](#)을 이해하기 쉽게 요약한 것입니다.

[Disclaimer](#)

이학박사 학위논문

# Engineering Structures and Properties of Nanomaterials for Biomedical and Device Applications

바이오의료 및 소자 응용을 위한 나노물질의  
구조와 특성 설계에 관한 연구

2020 년 8월

서울대학교 대학원

화학부 물리화학 전공

이 중 환

# Engineering Structures and Properties of Nanomaterials for Biomedical and Device Applications

Advisor : Prof. Byung Hee Hong

Submitting a Ph.D. Dissertation of Chemistry

August 2020

Graduate School of Natural Sciences

Seoul National University

Chemistry Major

Jong-Hwan Lee

Confirming the Ph.D. Dissertation written by

Jong-Hwan Lee

August 2020

Chair	이정호	(Seal)
Vice Chair	홍병희	(Seal)
Examiner	민광희	(Seal)
Examiner	고성표	(Seal)
Examiner	박종보	(Seal)

Abstract

**Engineering Structures and Properties of  
Nanomaterials for Biomedical and Device  
Applications**

Jong-Hwan Lee  
Department of Chemistry  
The Graduate School  
Seoul National University

Nanotechnology has been rapidly developed in recent years for various applications to biomedical, energy, display, and semiconductor industries. As the scale approaches quantum mechanical regime, the phenomena that can only be observed at 0, 1, and 2 dimensions become more important to understand and engineer the properties of nanomaterials. For example, 0D nanoparticles clearly show the band-gap depending their sizes, which often results in change of photoluminescent colors and photochemical reactivities. Besides, altered magnetic properties or enhanced catalytic properties are frequently observed in such nano-sized particles. On the other hand, the semiconductor quantum dots are being used in advanced in displays as highly efficient fluorescent layers, and the nanoparticle-based cathode materials are used to increase the capacity and the reliability of a lithium-ion battery. More recently, nanotechnology has been increasingly utilized for biomedical areas,

including drug delivery systems (DDS), contrast agents for MRI/PET, *etc.* In addition, the nanoparticle-based diagnostics tools and sensor devices are extensively studied for healthcare and wearable applications.

Since the current semiconductor devices are mostly processed in 2-dimension, a layered 2D film structures are favored for device applications, and the thin film technology used in semiconductor processing requires more and more nanotechnologies as the thickness approaches the atomic level. Therefore, understanding the physical and chemical properties of 2D materials depending on their number of layers, composition, defects, doping, and interface structures is of great importance as well to develop novel 2D material-based functional devices.

The 2-D nanomaterials represented by graphene have been intensively studied for recent decades for their outstanding electrical, photoelectronic, and mechanical properties. In particular, the graphene shows an outstanding stability and impermeability to reactive gases, which can be utilized as encapsulation layers that are essential in OLED displays and device packaging. In addition, transition metal dichalcogenides (TMDs) such as MoS<sub>2</sub> exhibit novel thickness dependent direct band-gaps that are useful in various optoelectronic devices, and the combination of those 2D materials with different properties is expected to be very useful to develop unique semiconductor devices. However, the interface between 2D semiconductor and electrodes in a field-effect transistor (FET), for example, considerably

affects the overall device performance, which needs to be optimized by tuning work functions or by controlling chemical composition at the interface.

In this thesis, the application of 0D nanoparticles and 2D semiconductors for drug delivery and transistor applications are described, respectively. Chapter 1 includes the theoretical background and the general applications of nanomaterials. Chapter 2 summarizes the results of biomedical applications of the nanoparticles loaded with drug molecules. The nanoparticles were synthesized by applying the growth principle of thin-film technology, and loaded with nucleic acids and anticancer substances for better stability during delivery *in vivo*. It was confirmed that the loaded materials are effectively transported into cancer cells and release the drug molecules to show the superior anticancer effect. Chapter 3 describes the synthesis and application of 2D molybdenum disulfide ( $\text{MoS}_2$ ) thin films for FETs with a gradient composition that can minimize the contact resistance. First, thin layers of Mo were deposited by thermal evaporation, followed by selective masking of the electrode areas with graphene as a gas-impermeable layer. Thereafter, the unmasked channel region was sulfurized by hydrogen sulfide ( $\text{H}_2\text{S}$ ) gas. As a result, only the exposed Mo surface was selectively transformed to  $\text{MoS}_2$ , where the gradient of chemical composition from Mo to  $\text{MoS}_2$  is formed at the interface. It was found that such gradual contact enables the smooth and successive change of work functions, lowered Schottky barriers, increased on-off ratio and charge carrier mobility.

In Chapter 4, the summary and conclusion of the thesis are depicted, finally.

**Keywords:** Nanotechnologies, nanoparticle, 2D materials, anti-cancer effect, chemical vapor deposition, transistor

**Student Number:** 2015-30978

---

## **Table of Contents**

---

<b>Abstract .....</b>	<b><i>i</i></b>
-----------------------	-----------------

<b>Table of Contents .....</b>	<b><i>v</i></b>
--------------------------------	-----------------

<b>List of Figures .....</b>	<b><i>vii</i></b>
------------------------------	-------------------

Chapter 1. Introducton .....	1
------------------------------	---

1. 1. 1. Background of 2D materials .....	3
---	---

1. 1. 2. Graphene .....	3
-------------------------	---

1. 1. 2. 1. Theoretical Background .....	3
--	---

1. 1. 2. 2. Applications .....	12
--------------------------------	----

1. 1. 3. Transition Metal Dichalcogenide (TMDC) .....	15
---	----

1. 1. 4. Chemical Vapor Deposition .....	18
--	----

1. 2. 1. Background of The Nanomedicine .....	22
---	----

1. 2. 2. Nanoparticles in The Nanomedicine .....	22
--	----

1. 2. 3. Electrical Devices in Bio-applications .....	26
---	----

Chapter 2. Development of Dual-pore Coexisting Branched Silica	
--	--

Nanoparticles for Efficient Gene-chemo Cancer Therapy

31

2. 1. Introduction .....	31
--------------------------	----



2. 2. Experimental .....	35
2. 3. Result and Discussion .....	43
2. 4. Conclusion .....	70
2. 5. References .....	71
Chapter 3. Graphene-Masked Selective Sulfurization of Mo Thin Films for High Performance Field-Effect Transistors ..	75
3. 1. Introduction .....	75
3. 2. Experimental .....	77
3. 3. Result and Discussion .....	80
3. 4. Conclusion .....	93
3. 5. References .....	95
Chapter 4. Conclusion .....	100
<b>Abstract (in Korean) .....</b>	<b>102</b>

## List of Figures

---

Figure 1.1. The lattice structure and the Brillouin zone of the graphene.

Figure 1.2. Scheme of the nearest-neighbor hopping in the graphene lattice

Figure 1.3. Three-dimensional electron energy structure at K point in the  
graphene

Figure 1.4. The scheme of the Hall conductivity in the single-layer graphene  
under the magnetic field.

Figure 1.5. Various applications of the graphene in the industrial fields.

Figure 1.6. Scheme of the bilayer graphene with various tilting angles. Moiré  
pattern was formed by a tilting angle and changed with a tilting  
angle. a) tilting angle:  $3^\circ$ , b) tilting angle:  $9^\circ$ , c) tilting angle:  $15^\circ$ ,  
d) tilting angle:  $30^\circ$ .

Figure 1.7. Atomic structure of the TMDCs (2H, 1T).

Figure 1.8. Scheme of the CVD.

Figure 1.9. Scheme of the chemical process in CVD

Figure 1.10. CALPHAD modeled the temperature-composition (T-x) phase  
diagram of MoS<sub>2</sub>. Reprinted from reference 16. Copyright 2016  
American Chemical Society.

Figure 1.11. CALPHAD modeled the temperature-pressure (T-P) phase  
diagram of MoS<sub>2</sub>. Reprinted from reference 16. Copyright 2016  
American Chemical Society.

Figure 1.12. Scheme of the MSN. a) image of the MSN. b) the MSN with drug which was loaded in the mesopore. c) drug release kinetic control via gate-keeping; various stimulus (pH, temperature, light) changed from off state to on state.

Figure 1.13. Various functional nanoparticles. a) Superparamagnetic iron oxide nanoparticle; spin orientation was ordered by magnetic field stimuli. b) Up-conversion nanoparticle with the core-shell structure; it absorbed the long-wavelength light, following irradiating the short-wavelength light.

Figure 1.14. Various electronics in bioapplication. a) Organ on a chip to be used MEMS technique, b) nanoneedle for drug screening, c) stem cell patterning by using photolithography, d) injectable electronics for monitoring brain dynamics, e) stretchable devices as smart healthcare device for glucose sensing and drug release, and f) nanopore for DNA sequencing; a - reprinted from reference 26, © 2020 NPG. b – reprinted from reference 30, © 2013 NPG. c – reprinted from reference 27, © 2015 NPG. d – reprinted from reference 29, © 2015 NPG. e – reprinted from reference 28, © 2017 American Association for the Advancement of Science. f – reprinted from reference 31, © 2011 NPG.

Scheme 2.1. The synthetic process and the controlled release of dual-cargos after cellular introduction. Disulfide bond in the DpSN was generated through the reaction between mercaptopropyl group and adamantanethiol. The controlled release of each cargo was accomplished by disulfide cleavage for the release of a small molecule in the middle box and anion exchange for the release of a nucleic acid in the right box.

Figure 2.1. Characterization of synthesized SpSN and DpSN. Transmission electron microscope (TEM) images of (a), (c) SpSN and (b), (d) DpSN. (e) Dynamic light scattering (DLS) measurement exhibited increased hydrodynamic diameter of DpSN from the formation of branched nanostructures. (f)  $\zeta$ -potential and average particle diameter from DLS measurement of SpSN and DpSN.

Figure 2.2. N<sub>2</sub> adsorption/desorption for characterization of pore size by Brunauer-Emmett-Teller (BET) method. Measured type-IV isotherm curves of adsorption volume (left) and calculated pore size distribution (right) of (a) DpSN and b) SpSN was represented.

Figure 2.3. Difference in secondary silica nanostructure formation against the surface moiety and existence of trisodium citrate additive. TEM images of (a) SpSN without surface functionalization and secondary nanostructure developed on (b) propyl-grafted SpSN, aminopropyl-grafted SpSN (c) without trisodium citrate, and (d)

with trisodium citrate additive. The images (e-h) at bottom implied higher magnification TEM images of (a-d), respectively

Figure 2.4. Characterization of the separately synthesized branched part of DpSN. a) low and high magnification images of the branched particle. b) the loading capacity of branched silica subunit nanoparticle against oligonucleotide (DNA-Cy5 and siRNA) was confirmed by gel-electrophoresis. c) isotherm curves, and d) the distribution of pore size data.

Figure 2.5. Characterization of conjugation of 1-adamantanethiol. a) UV-Vis spectrum; DTDP = 2,2'-dithiodipyridine solution, DpSN-P = 2-pyridinethiol conjugated DpSN, and Ada = 1-adamantanethiol solution. b) Size distribution of the particles.

Figure 2.6. Characterization of synthesized porous silica nanoparticles and non-porous silica nanoparticles. TEM images of a) non-porous silica nanoparticles and b) porous silica nanoparticles in low and high magnification, c) N<sub>2</sub> adsorption/desorption data plotting, and d) table of the information about silica nanoparticles depending on the presence or absence of porosity.

Figure 2.7. Loading and release profile of Cy5-DNA and Rho 6G as model cargos for SpSN and DpSN. (a) Release kinetics of the loaded Rho 6G was measured in 1X PBS solution in the presence of 10 mM dithiothreitol (DTT). (b) Loading capacities were calculated for

SpSN and DpSN. (c) Loading capacity of Cy5-DNA was evaluated by polyacrylamide gel electrophoresis (PAGE). (d) Confocal laser scanning microscope (CLSM) images of Cy5-DNA and/or Rho 6G loaded DpSN treated HeLa cells. Cell nuclei were stained with Hoechst 33342 (blue) before microscope observation. Scale bar is 25  $\mu$ m.

Figure 2.8. The colloidal stability of the SpSN, DpSN, and DpSN with capping was characterized by DLS measurement against 1 d incubation in 1x PBS and serum containing media.

Figure 2.9. Cytotoxicity of DpSN and SpSN was evaluated by MTT assay.

Figure 2.10. Fluorescent images of DpSN treated HeLa cells with Hoechst 33342 (Nuclei, blue), Calcein AM (Live, green), and EthD-1 (Dead, red) staining. Scale bar is 50  $\mu$ m.

Figure 2.11. Cytotoxicity of non-aminated SpSN was evaluated by MTT assay

Figure 2.12. Cy5-DNA loading capacity and release profile of SpSN and DpSN were calculated by PAGE. (a) loading capacity of Cy5-DNA towards SpSN and DpSN. Release profile of Cy5-DNA and/or Rho 6G from (b) DpSN and (c) SpSN.

Figure 2.13. The fluorescence microscope images of Cy5-DNA and/or Rho 6G loaded SpSN. It showed that SpSN could not exhibit the delivering capability against Cy5-DNA. ; a) control, b) DNA-Cy5 + SpSN complex, c) Rho. 6G + SpSN complex, and d) Rho. 6G + DNA

Cy-5 + SpSN complex. The scale bar is 25  $\mu$ m.

Figure 2.14. (a) Loading capacity and (b) releasing behavior of siRNA under various conditions were estimated by PAGE.

Figure 2.15. MTT cell viability assay against free Dox treatment in various concentrations.

Figure 2.16. Time-dependent release of Cy5-siRNA from FAM-DpSN was observed inside cells. The Cy5-siRNA loaded FAM-DpSN was shown as yellowish color by fluorescence signal superposition, and it gradually decreased over time due to Cy5-siRNA release (red) from FAM-DpSN (green). The scale bar is 100  $\mu$ m.

Figure 2.17. Pearson's correlation coefficient which indicates the overlapping area between FAM-DpSN and Cy5-siRNA was calculated. Pearson's correlation coefficient "1" indicates perfect overlap.

Figure 2.18. Fluorescent images of GFP expression in GFP-HeLa cells. (a) control, (b) siGFP + lipofectamine complex, and (c) siGFP + DpSN. The scale bar is 100  $\mu$ m.

Figure 2.19. Knockdown efficiency of GFP induced by siGFP was estimated by FACS. (a) control, (b) siGFP + lipofectamine complex, and (c) siGFP + DpSN. DpSN was more efficient in inducing GFP knockdown by siGFP than lipofectamine as a delivery carrier.

Figure 2.20. The quantitative therapeutic efficiency comparison. (a) MTT cell viability assay of free cargos, mono-modal therapy, and dual-

modal gene-chemo combinational therapy at 24 and 48 hr incubation against untreated cells (denoted as control). (b) Knockdown efficiency of Bcl-2 gene was validated by using RT-PCR with  $\beta$ -actin as housekeeping gene. (c) Fluorescent microscope images of live/dead stained HeLa cells. Nuclei (DAPI, blue), live cells (Calcein AM, green) and dead cells (EthiD-1, red) fluorescence signals and merged images exhibited combinational therapeutic efficiency. Scale bar is 200  $\mu$ m.

Figure 2.21. Live/dead staining mediated fluorescent images against gene or/and chemo treated cells. a) the Fluorescent images of the cell after 48 hr from treatment; Nuclei (DAPI, blue), live cells (Calcein AM, green) and dead cells (EthiD-1, red). Scale bar is 200  $\mu$ m. b) Quantitatively analyzed cell viability by using ImageJ program.

Table 2.1. N<sub>2</sub> adsorption/desorption data of SpSN, DpSN and separately prepared Branched part of DpSN was summarized.

Table 2.2. Zeta-potential of SpNP and DpSN against the loading of cargos.



Figure 3.1. Scheme of the device fabrication. a) procedure of the FET fabrication. b) schematic image of reaction between Mo film and  $\text{H}_2\text{S}$  precursor; the Mo film underneath graphene coating was effectively protected from sulfurization reaction, but exposed Mo film, which was not coated by graphene, reacted with  $\text{H}_2\text{S}$  gas. c) Optical microscope images of the FET device without  $\text{H}_2\text{S}$  treatment (left) and with  $\text{H}_2\text{S}$  treatment (right). Scale bar was 100  $\mu\text{m}$ .

Figure 3.2. Raman spectra with the various conditions; XL\_YYY  $^\circ\text{C}$  where X was the number of graphene layers and YYY was the synthetic temperature of sulfurization. a), b) and c) were Raman spectra of Mo film which was treated  $\text{H}_2\text{S}$  gas at various temperatures and coated by monolayer, bilayer, and 4 layers of graphene, respectively.

Figure 3.3. Raman spectra of graphene. a) Raman spectra of various layered graphene without  $\text{H}_2\text{S}$  treatment. b) Raman spectra of various layered graphene with  $\text{H}_2\text{S}$  treatment at 800  $^\circ\text{C}$ .

Figure 3.4. a) Raman spectra with various reaction temperatures; black line: 600  $^\circ\text{C}$ , red line: 700  $^\circ\text{C}$ , blue line: 800  $^\circ\text{C}$ , magenta line: 900  $^\circ\text{C}$ . b) Table of the full half maximum width with various reaction temperatures.

Figure 3.5. Characterization of field-effect transistor (FET) based on  $\text{MoS}_2$ . a)

Raman spectra of Mo film with various layers of graphene coating, after H<sub>2</sub>S treatment. b) XPS spectra of various conditions; 4L, 2L, 1L: 4-, bi-, and mono-layer graphene coating on Mo film with H<sub>2</sub>S treatment, respectively, MoS<sub>2</sub>: Mo film with H<sub>2</sub>S treatment, Mo: bare Mo film. c) Optical microscope image of FET; the red dashed rectangle was concerned with the Raman mapping region. d) Raman spectra of 1 (red line) and 2 (black line) region. e) Raman mapping images; the top and bottom images were formed by using MoS<sub>2</sub> Raman peak (A<sub>1g</sub> mode: 406 cm<sup>-1</sup>) and graphene Raman peak (2D peak: 2700 cm<sup>-1</sup>), respectively. Scale bar was 10 μm.

Figure 3.6. XPS of Mo film (black), Mo film with 4L graphene (red), H<sub>2</sub>S treated Mo film with 4L graphene. a) Mo binding range. b) sulfur binding range.

Figure 3.7. TEM images of Mo film with and without graphene, after H<sub>2</sub>S treatment. a) graphene coating on Mo film. b) H<sub>2</sub>S exposure region in Mo film without graphene. c) plan view image of the b) region. Inset: FFT pattern of the c). d) The interface between the exposed Mo region (without 4L graphene) and the protected Mo region with 4L graphene, after H<sub>2</sub>S treatment

Figure 3.8. STEM images of a) the H<sub>2</sub>S treated Mo film and b) interface between the Mo film with and without 4L graphene.

Figure 3.9. STEM images of plan view of MoS<sub>2</sub>.

Figure 3.10. a) I-V curve ( $I_{DS}$  vs.  $V_{DS}$ ) of the electrode region of MoS<sub>2</sub>-4L. b)

Optical images of FETs; left = MoS<sub>2</sub>-Au, right = MoS<sub>2</sub>-4L.

Figure 3.11. a) A schematic image of the EDLT based 4L graphene-coated MoS<sub>2</sub>

with ion gel. b) a schematic image of the EDLT during operating; when the gate voltage was applied, charged ion in ion gel was oriented by electrical gradient, and the electrical double layer was formed at the interface between MoS<sub>2</sub> and ion gel, which was a great dielectric layer.

Figure 3.12. Electrical properties of FET based on MoS<sub>2</sub>. a) Transfer curve ( $I_D$

vs.  $V_G$ ); the black line = MoS<sub>2</sub>-4L, the red line = MoS<sub>2</sub>-Au. b)

mobility of electron.  $V_{th}$  was extracted by linear fitting at the transfer curve of the decimal scale, followed by the extraction of the intercept value of the x-axis.  $V_{th}$  of MoS<sub>2</sub>-4L and MoS<sub>2</sub>-Au was

3.88 V and 3.71 V, respectively. The capacitance of ion gel was 7.2  $\mu$ F for electrons. c) output curve of MoS<sub>2</sub>-4L with various

conditions (from  $V_G = 0$  V to  $V_G$  4.5 V). d) output curve of MoS<sub>2</sub>-

4L with various conditions (from  $V_G = 0$  V to  $V_G$  4.5 V. Channel width and length of both of devices were 100  $\mu$ m and 80  $\mu$ m,

respectively.

# Chapter 1. Introduction

Nanotechnologies have been developed in two decades. Nanoparticles, such as quantum dots (QDs), have been commercially employed as materials for display and solar cell systems. Also, Lithium-ion battery has changed our lifestyle by enabling electronic devices to be portable.

In electronics, with the demand for smaller devices, nanotechnologies have become more important, and electronic components have also become nanosized. Especially, thin-film technologies, including chemical vapor deposition, physical vapor deposition, atomic layer deposition, molecular beam epitaxy, became more significant because it was directly connected with the quality, the number of processing steps, and price. Also, lithography and etching techniques have been developed for the fabrication of smaller devices.

Recently, various nanotechnologies, including complementary metal-oxide-semiconductor (CMOS), lithography, micro-electromechanical system (MEMS), nanoparticle, have been adopted into the biotechnologies. Nanoparticles have been studied for drug carrier system in the body, MEMS has been utilized in cell sorting system and body mimic cell culture system, and lithography has been facilitated as a tool of patterning of bio-molecule. Also, many researchers have focused on the CMOS technology owing to its ability to process the mass information, such as neuron-to-neuron interaction, drug screening.

Here, we introduce the theoretical background of two-dimensional materials, nanoparticles, and their application in nanomedical and device application. Then, the biological responses are reported when the nanoparticles are used as drug delivery system in the cancer cell. Finally, the field-effect transistor based on two-dimensional material is introduced, and chapter 4 summarized the conclusion.

### **1. 1. 1. Background of 2D materials**

Two-dimensional (2D) materials had an atomically thin structure, so that it had various exotic properties, including the absence of dangling bond, van der Waals interaction with other materials, finite length of the z-axis, and etc. Because of its unique properties, it enabled the discovery of new phenomena in solid-state physics, such as spin Hall effect (SPE), topological effect, integer quantum Hall effect, and etc.

Graphene was the first 2D materials, which consisted of only carbon atom, had a hexagonal ring, and had one atomic layer. After the discovery of graphene, other 2D materials had been discovered, including hexagonal boron nitride (h-BN), transition metal dichalcogenide (TMDC), black phosphorous, and MXene. Here, we introduce various 2D materials and their properties.

### **1. 1. 2. Graphene**

#### **1. 1. 2. 1 Theoretical Background**

Graphene was the first discovered-2D material, which consisted of only carbon and had a honeycomb structure. The electron of the carbon atom formed the  $sp^2$  orbital which was formed by hybridization of s and p orbital. This caused trigonal planar structure, and the  $\sigma$  bonding was formed between carbon atom while  $\pi$  bonding was formed between the remained p orbital of the carbon which was orthogonal to the in-plane.

Graphene has hexagonal lattice, and its lattice vectors and reciprocal lattice vectors were written as (1.1) (**Figure 1.1**);

$$a_1 = \frac{a}{2} (3, \sqrt{3}), a_2 = \frac{a}{2} (3, -\sqrt{3}), b_1 = \frac{2\pi}{3a} (1, \sqrt{3}), b_2 = \frac{2\pi}{3a} (1, -\sqrt{3}) \quad (1.1)$$

, where  $a (= 1.42 \text{ \AA})$  was the atomic distance between the carbon atom. The first Brillouin zone (FBZ) was shown as a hexagonal ring which was the same shape of the graphene lattice, but it was rotated with  $\pi/2$ . (Figure 1.1b) The six points in the FBZ was composed of two equivalent groups (K, K'), so that we can divide the graphene lattice into two sublattices;

$$K = \frac{2\pi}{3a} \left(1, \frac{1}{\sqrt{3}}\right), K' = \frac{2\pi}{3a} \left(1, -\frac{1}{\sqrt{3}}\right) \quad (1.2)$$

$$\delta_1 = \frac{a}{2} (1, \sqrt{3}), \delta_2 = \frac{a}{2} (1, -\sqrt{3}), \delta_3 = -a (1, 0) \quad (1.3)$$

, where  $\delta_i$  ( $i = \text{integer}$ ) was the nearest-neighbor vector.

Based on tight-binding (TB) approximation, the Hamiltonian for electron was represented by (1.4);

$$H = -t \sum_{\langle i,j \rangle, \sigma} (a_{\sigma,i}^\dagger b_{\sigma,j} + H.c.) - t' \sum_{\langle\langle i,j \rangle\rangle, \sigma} (a_{\sigma,i}^\dagger a_{\sigma,j} + b_{\sigma,i}^\dagger b_{\sigma,j} + H.c.) \quad (1.4)$$

,  $t$  ( $\approx 2.8 \text{ eV}$ ) was the hopping energy between the nearest-neighbor atom (corresponding to  $\delta_1, \delta_2, \delta_3$ ),  $t'$  was the hopping energy between the next nearest-neighbor atom (corresponding to  $a_1, a_2$ ),  $a_{\sigma,i}^\dagger$  ( $a_{\sigma,j}$ ) was the annihilation (creation) operator of the electron with  $\sigma$  spin on-site  $R_i$  on

sublattice A ( $b_{\sigma,i}^\dagger$  ( $b_{\sigma,j}$ ) was the same manner of  $a_{\sigma,i}^\dagger$  ( $a_{\sigma,j}$ ) on sublattice B).

The first term of the right side in Eq.1.4 was used as the electronic structure of the graphene with the nearest-neighbor hopping. (**Figure 1.2**) and the TB eigenfunctions was written as (1.5);

$$\begin{pmatrix} \alpha_k \\ \beta_k \end{pmatrix} = \sum_j \exp(ik) \cdot R_j^0 \begin{pmatrix} a_j^\dagger e^{-ik \cdot \delta_1/2} \\ b_j^\dagger e^{ik \cdot \delta_1/2} \end{pmatrix} \quad (1.5)$$

, where  $R_j^0$  was the reference point in the j cell.

When the electron at the A site jumped into the B site (including the opposite case), the Hamiltonian was represented by (1.6);

$$H = \begin{pmatrix} \epsilon_0 & -tf(k) \\ -tf^*(k) & \epsilon_0 \end{pmatrix}, f(k) = \sum_{l=1}^3 \exp(ik \cdot \delta_l) \quad (1.6)$$

, where  $\epsilon_0$  was zero. The energy, the eigenvalues of the Hamiltonian, was calculated by (1.7);

$$\epsilon_k = \pm t(1 + 4 \cos \frac{3k_x a}{2} \cos \frac{\sqrt{3}k_y a}{2} + 4 \cos^2 \frac{\sqrt{3}}{2} k_y a)^{1/2} \quad (1.7)$$

The condition where  $\epsilon_k$  was zero was represented by (1.8);

$$\frac{3k_x a}{2} = 2n\pi, \cos \frac{\sqrt{3}k_y a}{2} = -\frac{1}{2} \quad \text{or} \quad \frac{3k_x a}{2} = (2n+1)\pi, \cos \frac{\sqrt{3}k_y a}{2} = \frac{1}{2} \quad (n = \text{integer}) \quad (1.8)$$

This condition was satisfied at the K and K' point of the FBZ in the reciprocal space, and these were called Dirac point.

At near the Dirac point ( $K + q$ ,  $q \approx 0$ ), energy dispersion was represented by the expansion of  $-t \cdot f(k)$  in Eq.(1.9);



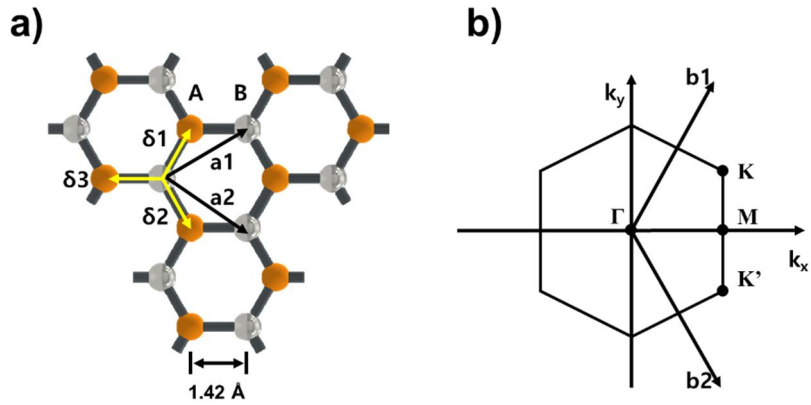


**Figure 1.1.** The lattice structure and the Brillouin zone of the graphene.

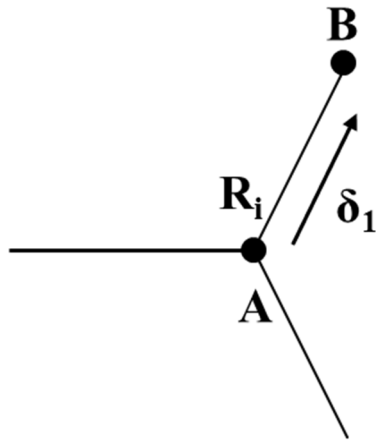


**Figure 1.2.** Scheme of the nearest-neighbor hopping in the graphene lattice

$$\epsilon(k) \cong 2te^{-iK_x a} q \cdot \nabla_k \left( e^{\frac{3ik_x a}{2}} \cos \frac{\sqrt{3}}{2} k_y a \right)_{k=K} = -\frac{3ta}{2} e^{-iK_x a} (iq_x - q_y) \quad (1.9)$$

With extraction of the constant factor  $(-i \cdot e^{-iK_x a})$ , Eq.1.9 was re-written as (1.10);

$$\epsilon(q) = \hbar v_F (q_x + iq_y) \left( 1 + O\left(\frac{q}{K}\right)^2 \right), v_F \equiv \frac{3ta}{2\hbar} \cong 10^6 \text{ m/sec} \quad (1.10)$$

, where  $\hbar$  was the reduced Planck constant, and  $v_F$  was the Fermi velocity of the electron. In the case at the K' point with the same manner of the K point, energy dispersion was represented by (1.11);

$$\epsilon(q) = \hbar v_F (q_x - iq_y) \left( 1 + O\left(\frac{q}{K}\right)^2 \right) = \epsilon^*(q) \quad (1.11)$$

, where the helicity was reversed. Therefore, the Hamiltonian was re-written as (1.12);

$$H \equiv \hbar v_F \begin{pmatrix} 0 & q_x + iq_y \\ q_x + iq_y & 0 \end{pmatrix} \equiv \hbar v_F \sigma \cdot q \quad (1.12)$$

, where  $\sigma$  was the Pauli matrix. The number of states at K point was  $q^2/2\pi$ , so that the density of states (DOS) was represented by (1.13);

$$\frac{dn_K(\epsilon)}{d\epsilon} = \frac{1}{\hbar v_F} \frac{dn_k(\epsilon)}{dq} = \frac{1}{\pi(\hbar v_F)^2} \epsilon \quad (1.13)$$

Because there were two Dirac points, the total DOS was twice the (1.13).

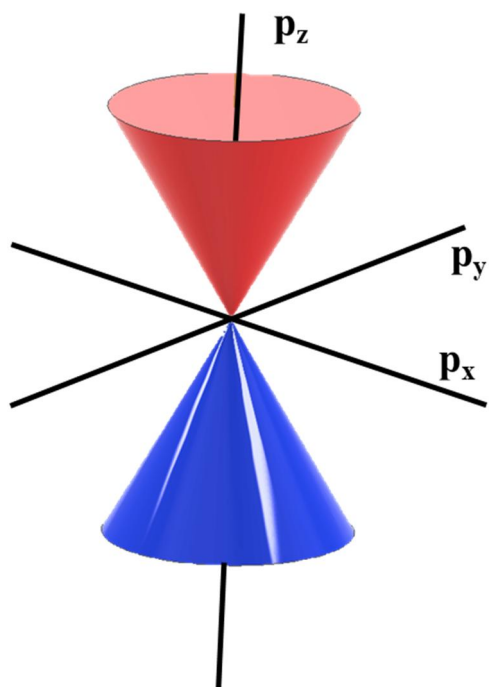


**Figure 1.3.** Three-dimensional electron energy structure at K point in the graphene

Without the magnetic field, the Hamiltonian was represented by (1.14);

$$H = \begin{pmatrix} 0 & v_F \sigma \cdot p \\ v_F \sigma \cdot p^\dagger & 0 \end{pmatrix} \quad (1.14)$$

, where  $p$  was the momentum operator. In the magnetic field, the  $p$  operator ( $\equiv i\hbar\nabla$ ) was changed into the  $\pi$  operator ( $\equiv i\hbar\nabla - \frac{e}{c}A$ ) (the gauge transformation), and the Hamiltonian was re-written as (1.15);

$$H = \begin{pmatrix} 0 & v_F \sigma \cdot \pi \\ v_F \sigma \cdot \pi^\dagger & 0 \end{pmatrix}, B = \text{curl } A \quad (1.15)$$

, where  $B$  was the magnetic field, and the  $A$  was the electro-magnetic potential vector. The commutator of the  $\pi_x$  and the  $\pi_y$  was represented by (1.16);

$$[\pi_x, \pi_y] = \frac{ie\hbar B_z}{c} \quad (1.16)$$

With the Landau gauge ( $A = (0, B_x, 0)$ ) and the variables ( $l_M \equiv \sqrt{\frac{c\hbar}{eB}}, \omega_0 \equiv \sqrt{2} \frac{v_F}{l_M}, \Pi_i \equiv \frac{l_M \pi_i}{\hbar}$ ), the Hamiltonian was re-written as (1.17);

$$H = \frac{\hbar\omega_0}{\sqrt{2}} \begin{pmatrix} 0 & \Pi_x + i\Pi_y \\ \Pi_x - i\Pi_y & 0 \end{pmatrix} \quad (1.17)$$

, and the  $\Pi$  operator was represented by (1.18) with  $l_M, \xi \equiv \frac{x}{l_M}, \eta \equiv \frac{y}{l_M}$ ;

$$\Pi_x = -i \frac{\partial}{\partial \xi}, \Pi_y = -i \frac{\partial}{\partial \eta} - \xi, [\Pi_x, \Pi_y] = i \quad (1.18)$$

$$H^2 = \frac{(\hbar\omega_0)^2}{2} \begin{pmatrix} \Pi_x^2 + \Pi_y^2 + 1 & 0 \\ 0 & \Pi_x^2 + \Pi_y^2 - 1 \end{pmatrix} \quad (1.19)$$

The  $\Pi_x^2 + \Pi_y^2 = -\frac{\partial^2}{\partial \xi^2} - \frac{\partial^2}{\partial \eta^2} + \xi^2$  was the Hamiltonian of a Harmonic oscillator. Therefore, the energy level of the electron in the magnetic field was represented by (1.20);

$$\epsilon_n = \pm \hbar \omega_0 \sqrt{n}, (n = integer) \quad (1.20)$$

, where n was the quantum number of the Landau level. Consequently, under the magnetic field, the energy level of the electron in the graphene was quantized, and the quantum spin Hall effect was observed. (**Figure 1.4**)

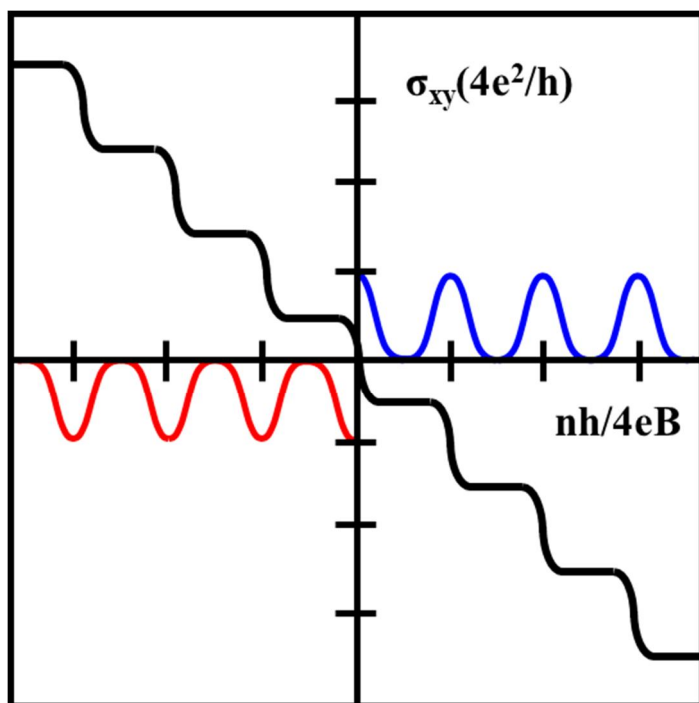


**Figure 1.4.** The scheme of the Hall conductivity in the single layer graphene under the magnetic field.

## **1. 1. 2. 2. Applications**

Graphene has been paid attention owing to its excellent electronic properties, mechanical properties, and thin feature. Especially, after the fabrication of the graphene monolayer via chemical vapor deposition (CVD) method,<sup>[1,2]</sup> application of the graphene in the electrical device has been explosively developed. The graphene has shown a potential of a transparent electrode instead of conventional indium titanium oxide (ITO) electrode due to its unique properties, including high mobility, low sheet resistance, and optical transparent by thin nature.<sup>[2]</sup> Also, it has been highlighted as the flexible electrode in the stretchable device because it satisfied high strength and bendability, as well as low resistance.<sup>[3]</sup>

Many researchers have been attracted by an exotic phenomena in the graphene.<sup>[4,5]</sup> In addition to a physical phenomenon, presented in the theoretical background, topological properties were observed due to the breaking of time-reversal symmetry (in case of the next-nearest-neighbor hopping).<sup>[5]</sup> Recently, in the case of the bilayer graphene, various results, including super-conductivity, were reported, which the Dirac cone in the K and K' points were overlapped, and the electronic structure was re-constructed by super-lattice from angle tilting between the graphene layers.<sup>[6]</sup>

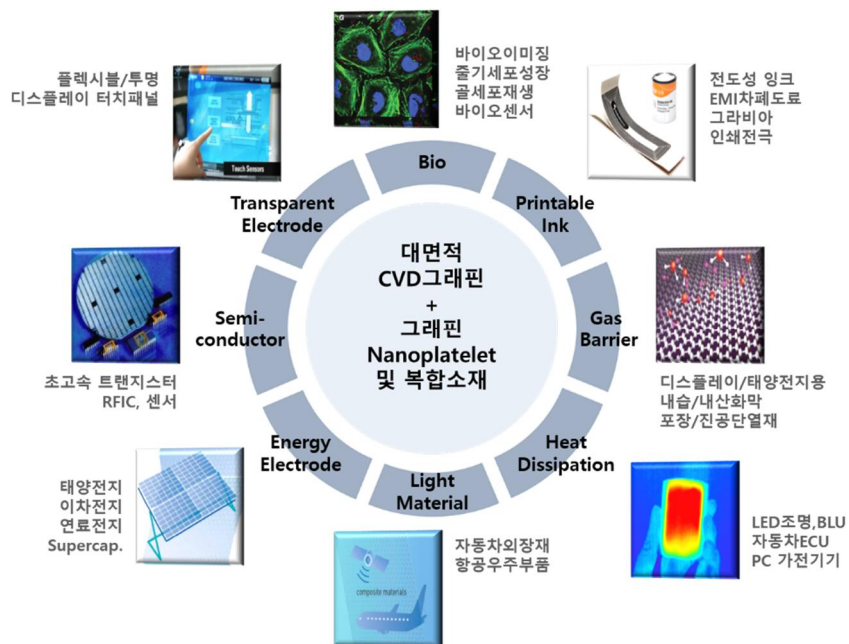


**Figure 1.5.** Various applications of the graphene in the industrial fields.



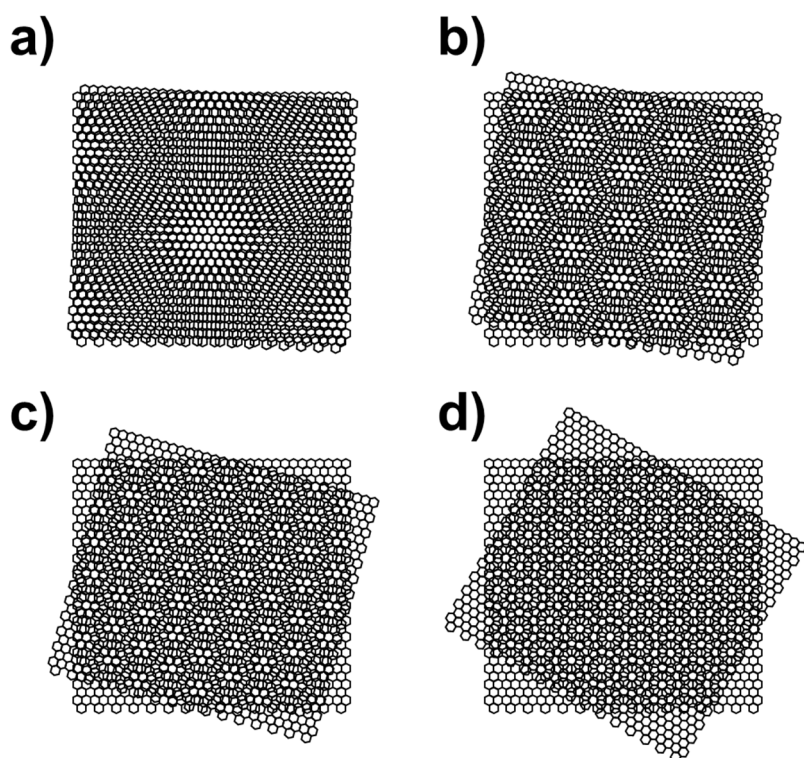


**Figure 1.6.** Scheme of the bilayer graphene with various tilting angles. Moiré pattern was formed by a tilting angle and changed with a tiling angle. a) tilting angle:  $3^\circ$ , b) tilting angle:  $9^\circ$ , c) tilting angle:  $15^\circ$ , d) tilting angle:  $30^\circ$ .

### 1. 1. 3. Transition Metal Dichalcogenide (TMDC)

TMDCs were other 2D materials, which consisted of transition metal atom and chalcogenide atom (S, Se, Te). Its formula was  $\text{MX}_2$  (M: Transition metal, X: chalcogen atom), and it was composed of 3 layers (X-M-X); bottom and top chalcogen layers, centered transition metal layer. Corresponding to atomic structure and d orbital of the transition metal, TMDCs had various properties, from metallic to insulating properties.<sup>[7]</sup>

Its atomic structure had two polytypes; trigonal prismatic (2H), octahedral (1T). **(Figure 1.7)** In the case of the trigonal prismatic, exotic properties were observed owing to inversion symmetry breaking. Recently, the Valleytronics which exploited the difference of K and K' points and had an additional degree of freedom had been paid attention in the quantum computing field.<sup>[8]</sup> When heterostructure of the TMDCs were formed, the recombination time of the exciton became longer, and the diffusion length of the exciton was able to be controlled.<sup>[9]</sup>

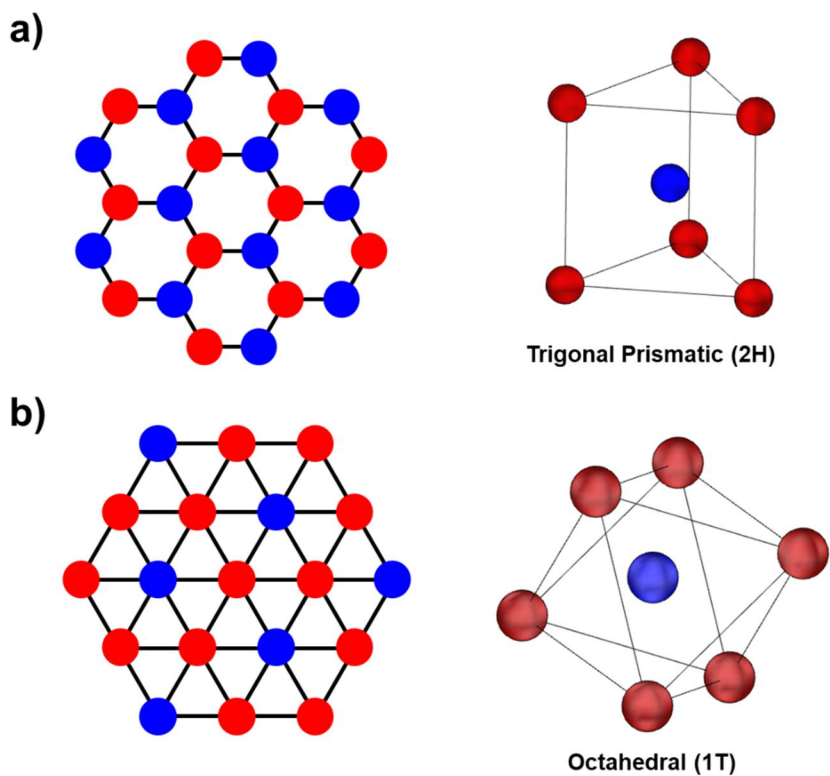


**Figure 1.7.** Atomic structure of the TMDCs (2H, 1T).

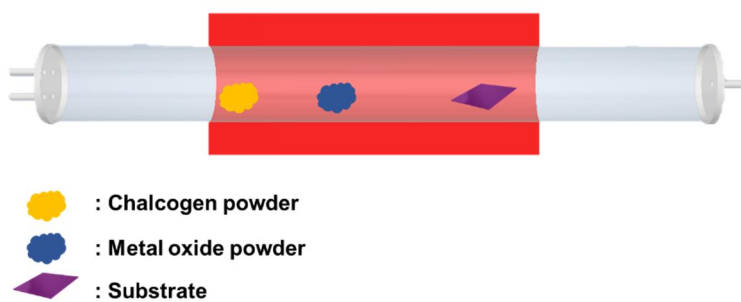


**Figure 1.8.** Scheme of the CVD.

TMDCs were normally obtained via CVD and mechanical exfoliation. CVD had been adopted as a bottom-up fabrication method of the TMDCs because it was feasible in mass production and quality control of the film. Generally, metal oxide precursor and chalcogen powder were used for the growth of the TMDCs, but that was limited by the high melting temperature of the metal oxide precursor. With NaCl salt, intermediate, metal oxy-halide, enabled to lower melting point of the metal precursor, so that various TMDCs were fabricated.<sup>[10]</sup> Additionally, TMDCs were fabricated with various methods, including metalorganic CVD (MOCVD),<sup>[11]</sup> sulfurization of metal thin film,<sup>[12]</sup> laser ablation,<sup>[13]</sup> wet chemical methods,<sup>[14]</sup> and etc.

In electrical devices, TMDCs had been highlighted as a next-generation semiconductor. It was able to overcome short channel effect because of short characteristic length from thin nature, the heavy effective mass of the electron;<sup>[15]</sup>

$$\lambda = \sqrt{\frac{\epsilon_s}{\epsilon_{ox}} t_s t_{ox}} \quad (1.20)$$

, where  $\epsilon_s$  and  $\epsilon_{ox}$  were the permittivity of the semiconductor and oxide at the gate, respectively,  $t_s$  and  $t_{ox}$  were the thickness of the semiconductor and the oxide, and  $\lambda$  was the characteristic length. Also, it had high mobility of the charge carrier, high on/off ratio, and small subthreshold swing. These features made the field-effect transistor (FET) based on TMDCs promising as next-generation electronics to overcome conventional barriers.

#### **1. 1. 4. Chemical Vapor Deposition**

CVD was one of the various methods of thin-film fabrication. In the CVD, precursor underwent the process; 1) Diffusion of the precursor into the boundary layer, 2) Adsorption onto the surface of the substrate, 3) Surface reaction and generation of the byproduct, 4) Surface diffusion. Through this process, the nucleation and growth took place.

In CVD, various parameters affected the growth of the TMDCs; precursor, concentration of the precursor, temperature, substrate, pressure during the reaction.<sup>[7]</sup> Basically, the precursor was directly connected with the final product. According to the atomic composition of the precursor or the phase of the precursor ( $\text{Mo(CO)}_6$ ,  $\text{H}_2\text{S}$ : gaseous precursors; sulfur (S), selenium (Se), transition metal oxide ( $\text{MoO}_3$ ,  $\text{WO}_3$ ), transition metal chloride ( $\text{MoCl}_5$ ,  $\text{WCl}_6$ : solid precursors), the condition of the nucleation and growth was quite different, so that it was the first option for the design of the fabrication.

The temperature was one of the main factors, by which kinetics and thermodynamics were governed. In the solid precursors, temperature affected the kinetics of the film growth in elevating the partial pressure of the precursor in the CVD chamber. Also, there was a specific stable phase depending on temperature, so that selecting the synthetic temperature had to be careful.<sup>[16]</sup>

**(Figure 1.10 and 1.11)**

Besides precursors and temperature, other parameters influenced the growth of the TMDCs in CVD. During the synthesis of the thin film, the

pressure was controlled by the flow rate of the gas mixture, such as carrier gas (inert gas),  $H_2$ , etc. As shown in **Figure 1.9**, gas flow enabled to affect the diffusion of the precursor and control the effective concentration of the precursors. Also, the substrate supplied the adsorption site of the precursor and it was able to catalyze the surface reaction. Therefore, in the case of the graphene, the number of layers were affected by types of the substrate.<sup>[17]</sup>

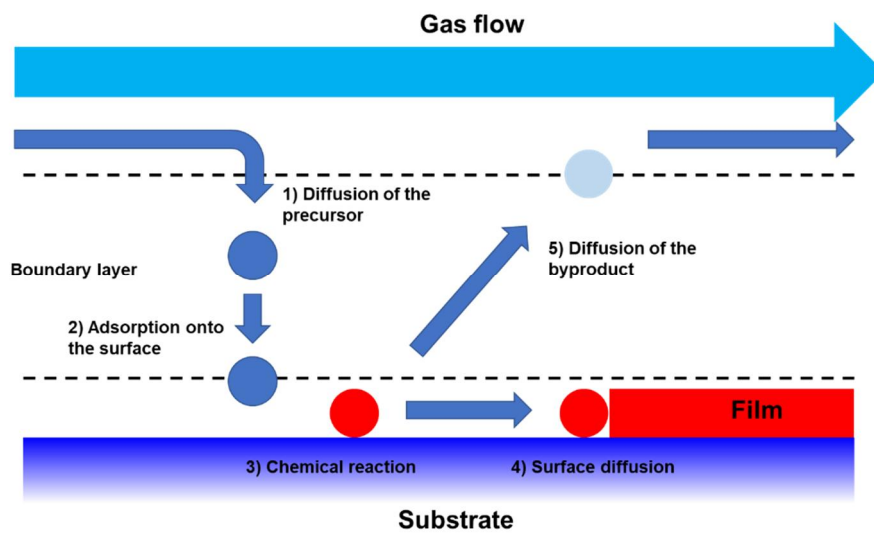


**Figure 1.9.** Scheme of the chemical process in CVD

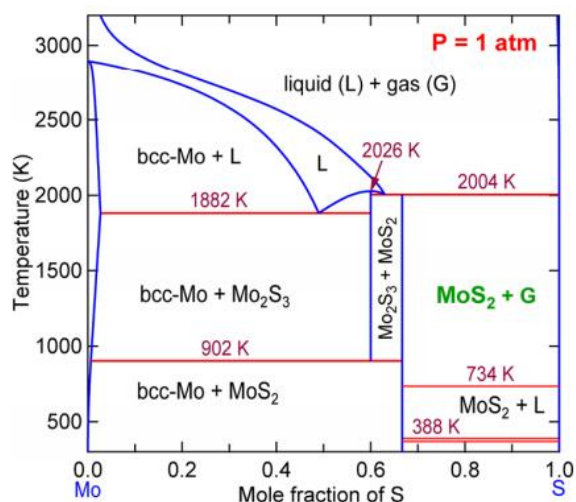


**Figure 1.10.** CALPHAD modeled the temperature-composition (T-x) phase diagram of MoS<sub>2</sub>. Reprinted from reference 16. Copyright 2016 American Chemical Society.

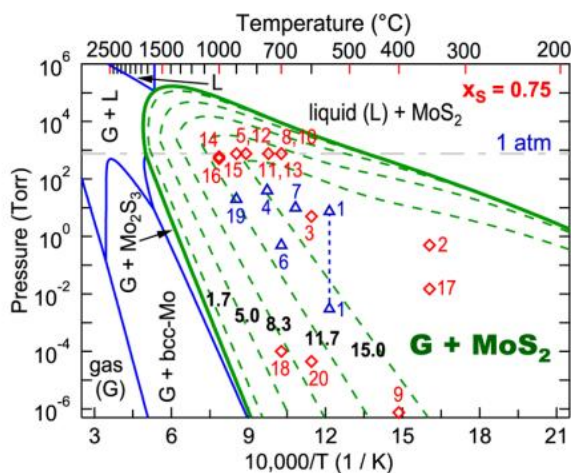


**Figure 1.11.** CALPHAD modeled the temperature-pressure (T-P) phase diagram of MoS<sub>2</sub>. Reprinted from reference 16. Copyright 2016 American Chemical Society.



### **1. 2. 1. Background of The Nanomedicine**

The application of nanomaterials in biomedical fields has been explosively studied in two decades. Nanoparticles have been highlighted as a nano-robot that implemented various duties (drug carrier, contrast reagent) in the body. Also, sensors based on electrical devices have mingled with nanotechnology (for example: nanoneedle for the detection of neuron signal, nanopore for the sequencing of the DNA). Here, we introduced the nanoparticle in the nanomedicine and the nanotechnological device in the bio-application.

### **1. 2. 2. Nanoparticles in The Nanomedicine**

Nanoparticles had a high surface to volume ratio, quantum confine effect, single grain, and various exotic properties, compared with bulk materials. Super-paramagnetism was observed in the  $\text{Fe}_2\text{O}_3$  nanoparticle,<sup>[18]</sup> the energy band was adjusted by controlling the particle size,<sup>[19]</sup> and catalytic properties were enhanced by a high density of the reactive site.<sup>[20]</sup> Also, the usage of the nanoparticle in bioapplication seemed to be reasonable because the size of the cell in the human body was micrometer scale.

Many researchers have tried to use the nanoparticle as drug carrier owing to its high surface area which enables to adsorb of the molecular drug. Among the nanomaterials, mesoporous silica nanoparticle (MSN) has been focused as drug carrier because it had high surface area from the mesoporous structure, biocompatibility, simple fabrication method. Its mesopore provided

the room for drug loading, an off-target release which caused the serious side effect of drug was lowered by gate capping via surface chemistry, and targeted-therapy was obtained through antibody conjugation onto the surface of the particle.<sup>[21]</sup>

With unique functionality, such as superparamagnetism, ultrasonic responsibility and upconversion of the infrared (IR) light,<sup>[22-24]</sup> the nanoparticles have been applied to contrast reagent. Iron oxide nanoparticle has been highlighted as the alternative of magnetic resonance imaging (MRI) contrast reagent and the up-conversion nanoparticle was used as imaging reagent in the cell. However, these nanoparticles generally induced foreign body response of the immune system. Recently, the side effects originated from the nanoparticle have been reported, so that these problems would have to be solved.<sup>[25]</sup>

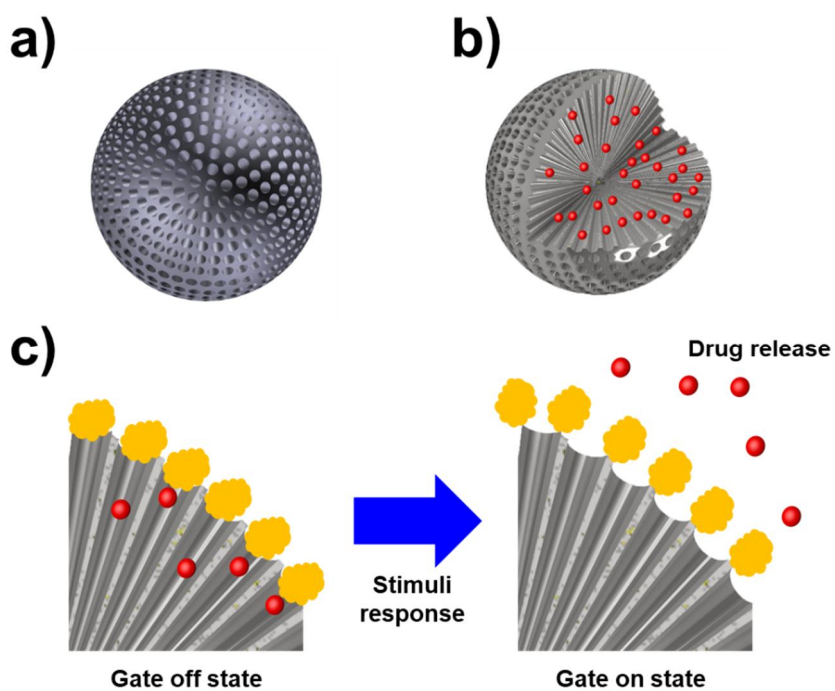


**Figure 1.12.** Scheme of the MSN. a) image of the MSN. b) the MSN with drug which was loaded in the mesopore. c) drug release kinetic control via gate-keeping; various stimulus (pH, temperature, light) changed from off state to on state.

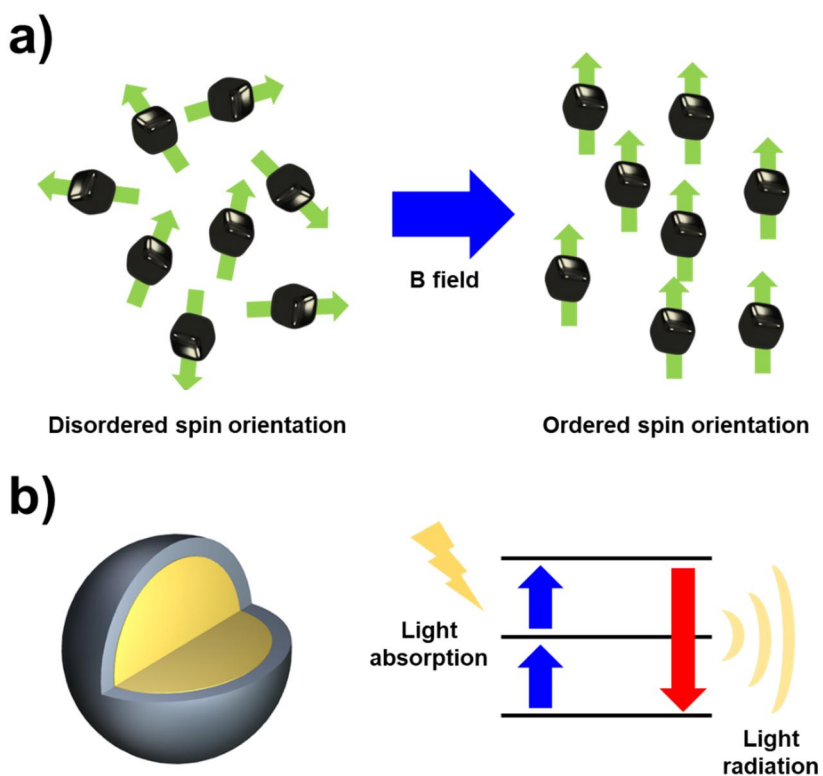


**Figure 1.13.** Various functional nanoparticles. a) Superparamagnetic iron oxide nanoparticle; spin orientation was ordered by magnetic field stimuli. b) Up-conversion nanoparticle with the core-shell structure; it absorbed the long-wavelength light, following irradiating the short-wavelength light.

### **1. 2. 3. Electrical Devices in Bio-applications**

Recently, various techniques of electrical device fabrication have been adopted to the bioapplication. Micro-electromechanical system (MEMS) was adopted as the fabrication of cell culture plate,<sup>[26]</sup> and lithography was facilitated in fabricating patterned-conjugation of bio-molecule.<sup>[27]</sup> Additionally, electrical devices have spread to bio-medical fields. Stretchable devices show potential for smart healthcare device to estimate the body signal such as glucose level, and the injectable device is highlighted as a tool of brain-computer interface.<sup>[28,29]</sup>

Nanoneedle and nanopore are the newly developed-electronic devices for biological applications. Nanoneedle has the nanosized-needle array which is a suitable tool as a needle for cells, and it has been applied to various fields, including molecule transfection, cell signal detection, and drug screening.<sup>[30]</sup> A nanopore is the promising DNA sequencing technology.<sup>[31]</sup> It consisted of the two electrodes and the membrane with nanopore which was located between the two electrodes, and the change of the ionic current was observed when bio-molecule passed through the nanopore of the membrane. Furthermore, various technologies in electronics emerged, combined, mingled, adopted to bioapplications.

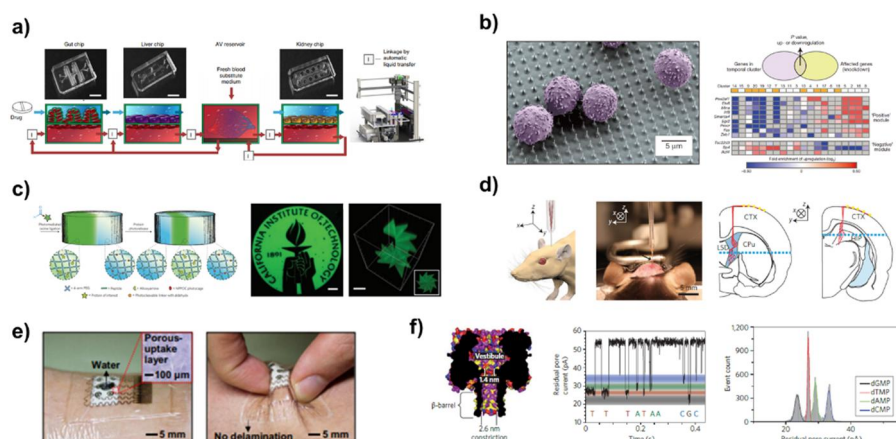


**Figure 1.14.** Various electronics in bioapplication. a) Organ on a chip to be used MEMS technique, b) nanoneedle for drug screening, c) stem cell patterning by using photolithography, d) injectable electronics for monitoring brain dynamics, e) stretchable devices as smart healthcare device for glucose sensing and drug release, and f) nanopore for DNA sequencing; a - reprinted from reference 26, © 2020 NPG. b – reprinted from reference 30, © 2013 NPG. c – reprinted from reference 27, © 2015 NPG. d – reprinted from reference 29, © 2015 NPG. e – reprinted from reference 28, © 2017 American Association for the Advancement of Science. f – reprinted from reference 31, © 2011 NPG.

### 1. 3. References

- [1] K. S. Kim, Y. Zhao, H. Jang, S. Y. Lee, J. M. Kim, K. S. Kim, J.-H. Ahn, P. Kim, J.-Y. Choi, B. H. Hong *Nature* **2009**, *457*, 706
- [2] S. Bae; H. Kim; Y. Lee; X. Xu; J.-S. Park; Y. Zheng; J. Balakrishnan; T. Lei; H. R. Kim; Y. I. Song; Y.-J. Kim; K. S. Kim; B. Özyilmaz; J.-H. Ahn; B. H. Hong; S. Lijima *Nat. Nanotechnol* **2010**, *5*, 574-578
- [3] H. Jang, Y. J. Park, X. Chen, T. Das, M.-S. Kim, J.-H. Ahn *Adv. Mater.* **2016**, *28*, 4184-4202
- [4] K. S. Novoselov, E. McCann, S. V. Morozov, V. I. Fal'ko, M. I. Katsnelson, U. Zeitler, D. Jiang, F. Schedin, A. K. Geim *Nat. Phys.* **2006**, *2*, 177
- [5] D. J. Rizzo, G. Veber, T. Cao, C. Bronner, T. Chen, F. Zhao, H. Rodriguez, S. G. Louie, M. F. Crommie, F. R. Fischer *Nature* **2018**, *560*, 204
- [6] Y. Cao, V. Fatemi, S. Fang, K. Watanabe, T. Taniguchi, E. Kaxiras, P. Jarillo-Herrero *Nature* **2018**, *556*, 43
- [7] Z. Cai, B. Liu, X. Zou, H.-M. Cheng *Chem.Rev.* **2018**, *118*, 6091-6133
- [8] K. F. Mak, K. I. McGill, J. Park, P. L. McEuen *Science* **2014**, *344*, 1489
- [9] D. Unuchek, A. Ciarrocchi, A. Avsar, Z. Sun, K. Watanabe, T. Taniguchi, A. Kis *Nat. Nanotechnol.* **2019**, *14*, 1104-1109
- [10] J. Zhou, J. Lin, X. Huang, Y. Zhou, Y. Chen, J. Xia, H. Wang, Y. Xie, H. Yu, J. Lei, D. Wu, F. Liu, Q. Fu, Q. Zeng, C.-H. Hsu, C. Yang, L. Lu, T. Yu,

- Z. Shen, H. Lin, B. I. Yakobson, Q. Liu, K. Suenaga, G. Liu, Z. Liu *Nature* **2018**, *556*, 355-359
- [11] S. Cwik, D. Mitoraj, O. M. Reyes, D. Rogalla, D. Peeters, J. Kim, H. M. Schütz, C. Bock, R. Beranek, A. Devi *Adv. Mater. Interfaces* **2018**, *5*, 1800140
- [12] Y. Lee, J. Lee, H. Bark, I.-K. Oh, G. H. Ryu, Z. Lee, H. Kim, J. H. Cho, J.-H. Ahn, C. Lee *Nanoscale* **2014**, *6*, 2821-2826
- [13] B. Li, L. Jiang, X. Li, P. Ran, P. Zuo, A. Wang, L. Qu, Y. Zhao, Z. Cheng, Y. Lu *Sci. Rep.* **2017**, *7*, 11182
- [14] J.-B. Lee, Y. R. Lim, A. K. Katiyar, W. Song, J. Lim, S. Bae, T.-W. Kim, S.-K. Lee, J.-H. Ahn *Adv. Mater.* **2019**, *31*, 1904194
- [15] H. Liu, A. T. Neal, P. D. Ye *ACS Nano* **2012**, *6*, 8563-8569
- [16] S.-L. Shang, G. Lindwall, Y. Wang, J. M. Redwing, T. Anderson, Z.-K. Liu *Nano Lett.* **2016**, *16*, 5742-5750
- [17] T. Lin, F. Huang, D. Wan, H. Bi, X. Xie, M. Jiang *Nanoscale* **2013**, *5*, 5847-5853
- [18] J. Park, K. An, Y. Hwang, J.-G. Park, H.-J. Noh, J.-Y. Kim, J.-H. Park, N.-M. Hwang, T. Hyeon *Nat. Mater.* **2004**, *3*, 891
- [19] L. Li, J. Hu, W. Yang, A. P. Alivisatos *Nano Lett.* **2001**, *1*, 349-351
- [20] B. Ni, X. Wang *Adv. Sci.* **2015**, *2*, 150085
- [21] I. I. Slowing, J. L. Wivero-Escoto, C.-W. Wu, V. S.-Y. Lin *Adv. Drug Deliver. Rev.* **2008**, *60*, 1278-1288



- [22] S. K. Maji, S. Sreejith, J. Joseph, M. Lin, T. He, Y. Tong, H. Sun, S. W.-K. Yu, Y. Zhao *Adv. Mater.* **2014**, *26*, 5633-5638
- [23] F. Li, Z. Liang, J. Liu, J. Sun, X. Hu, M. Zhao, J. Liu, R. Bai, D. Kim, X. Sun, T. Hyeon, D. Ling *Nano Lett.* **2019**, *19*, 4213-4220
- [24] N. T. Blum, A. Yildirim, C. Gyorkos, D. Shi, A. Cai, R. Chattaraj, A. P. Goodwin *ACS Appl. Mater. Interfaces* **2019**, *11*, 15233-15240
- [25] S. R. MacEwan, A. Chilkoti *Angew. Chem. Int. Ed.* **2017**, *56*, 6712-6733
- [26] B. Zhang, A. Korolj, B. F. L. Lai, M. Radisic *Nat. Rev. Mater.* **2018**, *3*, 257
- [27] C. A. DeForest, D. A. Tirrell *Nat. Mater.* **2015**, *14*, 523
- [28] H. Lee, C. Song, Y. S. Hong, M. S. Kim, H. R. Cho, T. Kang, K. Shin, S. H. Choi, T. Hyeon, D.-H. Kim *Sci. Adv.* **2017**, *3*, e1601314
- [29] J. Liu, T.-M. Fu, Z. Cheng, G. Hong, T. Zhou, L. Jin, M. Duvvuri, Z. Jiang, P. Kruskal, C. Xie, Z. Suo, Y. Fang, C. M. Lieber *Nat. Nanotechnol.* **2015**, *10*, 629
- [30] C. Chiappini *ACS Sens.* **2017**, *2*, 1086-1102
- [31] B. M. Venkatesan, R. Bashir *Nat. Nanotechnol.* **2011**, *6*, 615

## **Chapter 2. Development of Dual-pore Coexisting Branched Silica Nanoparticles for Efficient Gene-chemo Cancer Therapy**

### **2. 1. Introduction**

Biomedical application of nanomaterials is one of the research topics that has received enormous attention for decades. However, heterogeneous environment and somatic mutation of cancer cell are main problems in anti-cancer therapy. These problems have single small molecule therapy ineffective, and tumor cells become drug-resistance tumor cell, resulting in the needs of higher dose of drug or other therapy.<sup>[1]</sup> Gene therapy is another approach for anticancer therapy, which use the genetic material, such as plasmid, siRNA, and DNA. However, single gene therapy may be insufficient for cancer therapy.<sup>[2]</sup> Gene-chemo therapy, one of combination therapy, would be appropriate approach because target different pathways, which may induce synergetic anti-cancer effect.

To prepare multi-functional nanomaterials for targeting multiple pathways, one of the approaches is hybrid nanoparticle, which is being spotlighted in application fields such as drug delivery,<sup>[3,4]</sup> bio-imaging,<sup>[5-7]</sup> immunotherapy and cancer therapy.<sup>[8-11]</sup> Beyond the simple biomedical applications, the hybrid nanoparticles including metal-metal and metal-metal

oxide nanocomposites which guaranteed complex functionality can be used to realize more efficient applications, for example, multi-type drug delivery,<sup>[3,4]</sup> chemo-thermo combinational therapy and implementation of orthogonal imaging strategies for enhanced resolution.<sup>[5-9]</sup> Among them, multi-type drug delivering strategy for single disease target was regarded as promising approach to treat multi-drug resistance infected cells which commonly occurred *via* mutation.<sup>[12-14]</sup>

Here, we reported the development of the dual-structured porous silica nanoparticles (DpSN) to accomplish hybrid nanoparticle mediated drug-gene dual-modal delivery for treating cancer. To enable proposed platform, hybrid nanostructure that can interact independently with two distinctive cargo, nucleic acid (small interfering RNA to knockdown B cell lymphoma 2 (Bcl-2), siBcl-2) and anticancer drug (doxorubicin, Dox), was required. To accomplish the suggested dual-modal delivery kinetics, hybrid nanoparticle DpSN was designed and prepared by conventional Stöber method and following Volmer-Weber growth (VW growth).<sup>[10,15-17]</sup> Two main domains of DpSN consisted of i) positively charged core nanostructure with a large pore diameter to load relatively bulky and negatively charged siRNA and ii) negatively charged branched nanostructure with a small pore diameter for doxorubicin loading with capping through the interaction between 1-adamantanthiol and  $\beta$ -cyclodextrin. By using the loading and release profile of model cargos, cyanine dye 5 fluorescently labelled DNA (Cy5-DNA) and rhodamine 6G (Rho 6G), we

successfully demonstrated the feasibility of dual-modal drug delivery. Finally, we successfully showed therapeutic efficacy of the dual-modal drug delivery against human cervical cancer cell line HeLa *via* the combinational chemotherapy of Bcl-2 siRNA and Dox *in vitro*.



## 2. 2. Experimental

*Materials:* Hexadecyltrimethylammonium bromide (CTAB,  $\geq 99\%$ ) was purchased from Acros (New Jersey, USA). (3-Aminopropyl)triethoxysilane (APTES,  $\geq 98\%$ ), Tetraethyl orthosilicate (TEOS,  $98\%$ ), Tetramethyl orthosilicate (TMOS,  $98\%$ ), n-Propyltriethoxysilane (PTES,  $97\%$ ), (3-Mercapropyl)triethoxysilane (MPTES,  $\geq 80\%$ ), 1-Adamantanethiol ( $95\%$ ), 2,2'-dithiodipyridine ( $98\%$ ), 3-(4,5-Dimethylthiazol-2-yl)-2,5-Diphenyltetrazolium Bromide (MTT,  $98\%$ ), doxorubicin hydrochloride (DOX), heparin sodium salt from porcine intestinal mucosa (heparin,  $\geq 180$  USP units/mg), and sodium citrate tribasic hydrate (citrate,  $\geq 99\%$ ) were purchased from Sigma-Aldrich (St. Louis, MO, USA). Urea ( $99.0\%$ ), sodium hydroxide (NaOH,  $\geq 97\%$ ) and Ethyl acetate (EA,  $\geq 99.5\%$ ) were purchased from Junsei Chemical Co. (Tokyo, Japan). Methanol (MeOH,  $\geq 99.5\%$ ), ethanol (EtOH,  $95\%$ ), ammonium hydroxide (NH<sub>4</sub>OH,  $25\text{--}28\%$ ), toluene ( $\geq 99.5\%$ ), isopropyl alcohol (IPA,  $99.5\%$ ), acetone ( $99.5\%$ ), and hydrogen chloride ( $\geq 35\%$ ) were purchased from Daejung chemical & metal Co. (Shiheung, Korea). LIVE/DEAD viability/cytotoxicity Assay kit was purchased from Molecular Probes Inc. (Eugene, OR, USA). Deionized water (DI water, Millipore, Bedford, MA, USA,  $18.2\text{ M}\Omega\cdot\text{cm}$  resistivity) was used without further purification. Dulbecco's Modified Eagle's Medium (DMEM), fetal bovine serum (FBS) and Phosphate buffered saline (PBS, pH 7.4) were purchased from WelGENE Inc (Daegu, Korea). siGFP, siRNA-Cy5 and siBcl-2 were purchased from Bioneer

Inc. (Daejeon, Korea). DNA-Cy5 and PCR primers related to Bcl-2, GFP, and beta-actin gene were purchased from Genotech. Inc. (Daejeon, Korea).

*Synthesis of the SpSN:* SpSN was prepared by modified Stöber method.<sup>[40]</sup> Briefly, CTAB (1.3 mmol) and Urea (0.5 mmol) were dissolved in DI water (15 mL) and toluene (15 mL), followed adding IPA (6 mmol). The solution was vigorously stirred and TEOS (6 mmol) was added by dropwise in solution, followed by stirring for 30 min at room temperature. Then, the reaction was kept at 70 °C for 16 hr. The product was washed with the mixture of acetone and water several times. Finally, remaining CTAB was removed by calcination at 550 °C for 5 hr.

*SpSN surface amination:* As-prepared SpSN (30 mg) was dispersed in EtOH (10 mL) and the precursor (1 mL) containing a functional group (APTES and PTES) was sequentially added to the solution under vigorous stirring at 80 °C for overnight. The SpSN was purified by centrifugation with EtOH, after the reaction.

*Synthesis of the DpSN using citrate solution:* The SpSN (30 mg) was dispersed in EtOH (10 mL). CTAB solution (2 mL, 54.8 mM), NH<sub>4</sub>OH (0.75 mL) and citrate solution (0.3 mL, 38.8 mM) were sequentially added in DI water. The colloidal solution of the SpSN was added in the solvent mixture, followed by

addition of the mixture of MPTES and TEOS (total volume of that was 0.12 mL and the volume ratio of MPTES-to-TEOS was 5:95).

*Synthesis of the branched part without the core part:* The branched part without the core part was synthesized using solution without the corepart, in the same manner of synthesizing of the DpSN.

*Synthesis of the porous silica and non-porous silica:* porous silica was synthesized by following the reference.<sup>[42]</sup> CTAB and 1 M NaOH solution was added to the mixture of DI water (460 mL) and MeOH (420 mL) under vigorous stirring for 10 min. Then, TMOS (1.3 mL) was added to the reaction solution for 8 hr under vigorous stirring, followed by aging overnight.

*Synthesis of the non-porous silica:* non-porous silica was synthesized by following the reference.<sup>[44]</sup> The reaction solution was prepared by mixing EtOH (100 mL), DI water (1.8 mL), and NH<sub>4</sub>OH (0.591 mL) under vigorous stirring for 5 min. After mixing the solution, TEOS (6.026 mL) was added into the reaction solution for 24 hr.

*CTAB removal:* CTAB in the DpSN was extracted by HCl. HCl (5mL) was added into the colloidal solution of the particle (EtOH, 20 mL) under vigorous stirring at 80 °C for overnight.



*Capping of the DpSN:* The capping method was prepared by following the reference.<sup>[41]</sup> First of all, the DpSN (100 mg) was dispersed in MeOH (25 mL). The solution was reacted with 2,2'-dithiodipyridine (600 mg) for 24 hr under dark. Secondly, the solution was rinsed at several times by MeOH and re-dispersed in MeOH (10 mL), followed by stirring overnight after adding 1-adamantane (100 mg). Then, after washed by EtOH, the solution was dispersed in 1X PBS and reacted with  $\beta$ -cyclodextrin (30 mg) overnight.

*FAM-conjugated DpSN:* The DpSN-FAM was synthesized by following the reference.<sup>[43]</sup> The DpSN (30 mg) was dispersed in DI water (1 mL), followed by adding the FAM-NHS solution (10  $\mu$ L, 2.5 mg/mL in DMSO). The complex reacted under the dark condition during the overnight.

*Characterization:* Transmission electron microscopy (TEM) experiments were performed with a H-7600 (Hitachi, Japan) at 100 KeV and LIBRA 120 (Carl Zeiss, Germany) at 120 KeV. Zeta-potential and dynamic light scattering (DLS) data were obtained by Zetasizer NanoS (Malvern instruments, United Kingdom). The fluorescence images were observed by a Ti inverted fluorescence microscopy equipped with a 4x objective IX 71 (Olympus, Japan) and a Cpp;SNAPcf charge coupled device (CCD) camera (Photometrics, USA) with Metamorph image analysis software (Molecular Devices, CA).

*Cell culture:* HeLa cells and GFP-HeLa cells were cultured in DMEM containing D-glucose ( $4.5 \text{ g L}^{-1}$ ) and supplemented with 10 % FBS, penicillin ( $100 \text{ units mL}^{-1}$ ), and streptomycin ( $100 \text{ g mL}^{-1}$ ). Cells were maintained in a humidified incubator under 5 %  $\text{CO}_2$  at  $37^\circ\text{C}$ .

*Confocal image:* HeLa cells were seeded in 4-well glass chamber slide at the density of  $5 \times 10^4$  per well. After 24 hr, cells were treated with the DpSNs ( $20 \mu\text{g}$ ) and the SpSNs ( $20 \mu\text{g}$ ) containing Rho. 6G, DNA-Cy5 ( $25 \text{ pmol}$ ) and Rho. 6G ( $1 \mu\text{g}$ ) + DNA-Cy5 ( $25 \text{ pmol}$ ) for 4 hours in humidified incubator under the serum-free media. Then, the cell was incubated in the serum-containing medium for 24 hours after removing the medium and washing with 1X PBS solution. A nucleus of the cell was stained by Hoechst 33342 solution prior to observation. Confocal images were acquired with DeltaVision Elite High Resolution Microscope (GE Healthcare, United Kingdom) equipped with 60 X objective lens (Olympus, Japan).

*The release of the siRNA:* HeLa cells were seeded in 96-well cell culture plate at the density of  $1 \times 10^4$  per well. After 24 hr, the cells were treated with the group A (DpSN :  $10 \mu\text{g}$ , siRNA-Cy5 :  $12.5 \text{ pmol}$ ) and the group B (DpSN :  $10 \mu\text{g}$ , siRNA-Cy5 :  $12.5 \text{ pmol}$ , DOX :  $50 \text{ pmol}$ ) under the serum free condition for 4 hr. After incubation, the medium was removed, and the complete medium

was added to each well. The release of the siRNA in the cells were observed via Ti inverted fluorescence microscopy. Then, Pearson's correlation coefficient was calculated by the ImageJ software.

*Estimation of knock-down efficiency:* HeLa cells were seeded in 24-well cell culture plate at the density of  $3 \times 10^4$  per well. After 24 hr, the cells were treated with the DpSN-siGFP (DpSN : 20  $\mu$ g, siGFP : 25 pmol) in the same manner of the experiment of confocal image. Knock-down efficiency was confirmed by a Ti inverted fluorescence microscopy and BD Bioscience FACSCanto (BD Bioscience, USA), after 24 hours from the particle treatment.

*Cell viability test:* HeLa cells were seeded in the 96-well cell culture plate at the density of  $1 \times 10^4$  per well. The efficiency of siBcl-2 (12.5 pmol), DOX (50 pmol), and siBcl-2 + DOX (siBcl-2 : 12.5 pmol, DOX : 50 pmol) groups which were loaded into the DpSN (10  $\mu$ g) or not was estimated by the MTT assay in triplicate. In the same manner, HeLa cells seeded in 24-well cell culture plate at the density of  $3 \times 10^4$  per well were treated with them. Then, a nucleus of the cell was stained with DAPI, followed the cell stained by LIVE/DEAD kit based on the manufacturer's protocol. The fluorescence images was obtained through a Ti inverted fluorescence microscopy.

*RT-PCR*: HeLa cells were seeded in 6-well cell culture plate at the cell density of  $1 \times 10^5$  per well. Cells were treated with the groups of siBcl-2, siBcl-2 + DOX, the DpSN-siBcl-2, the DpSN-siBcl-2-DOX, and the DpSN without cargoes in the same manner of the experiment of confocal image. After 24 hr, total RNA was extracted by TRIZOL reagent according to the previous reference.<sup>[42]</sup> RT-PCR was carried out using a Super-script<sup>TM</sup> II RT kit. Thermal cycling condition was governed by the condition, as represented the recipe: 1) cDNA synthesis; 1 cycle at 65 °C for 5 min, 42 °C for 2 min, 42 °C for 50 min and 70 °C for 15 min, 2) PCR for Bcl-2 gene: 1 cycle at 95 °C for 4 min, 30 cycle at 95 °C for 30 sec, 50 °C for 30 sec and 72 °C for 30 sec, 1 cycle at 72 °C for 10 min, 3) PCR for beta-actin: 1 cycle at 94 °C for 5 min, 35 cycle at 94 °C for 30 sec, 50 °C for 30 sec and 72 for 30 sec, 1 cycle 72 °C for 5 min.

## 2. 3. Result and Discussion

First, seed porous silica nanoparticle (SpSN) as supporting core for hybrid nanoparticle preparation was synthesized by previously established Stöber method with slight modification.<sup>[18]</sup> Synthesized SpSN was further chemically modified by (3-aminopropyl)triethoxysilane (APTES) to introduce amine functional groups, enabling electrostatic interaction mediated oligonucleotide loading later. According to the transmission electron microscopy (TEM) and dynamic light scattering (DLS) observation, prepared monodispersed SpSN exhibited average diameter of 280.4 nm with wrinkled cross-sectional morphology. **(Figure 2.1a,b,e)** Next, DpSN was synthesized by VW growth from aminated SpSN as a template. Briefly, addition of growth precursor (3-mercaptopropyl)triethoxysilane (MPTES) and tetraethyl orthosilicate (TEOS) mixture in appropriate ratio under the existence of surfactant and base in ethanolic solvent induced branched substructure growth on the SpSN template. Monodisperse branched morphology of DpSN which observed from TEM images and measured hydrodynamic radius of 368.0 nm clearly supported successful preparation of hybrid porous silica nanoparticles. **(Figure 2.1c,d,e)**  $\zeta$ -potential of DpSN ( $31.2 \pm 0.5$  mV) was lower than that of SpSN ( $41.5 \pm 0.6$  mV). **(Figure 2.1f)** The change in  $\zeta$ -potential could be originated from the abundant hydroxyl (-OH) and thiol (-SH) functional groups on the surface of newly formed branched region.

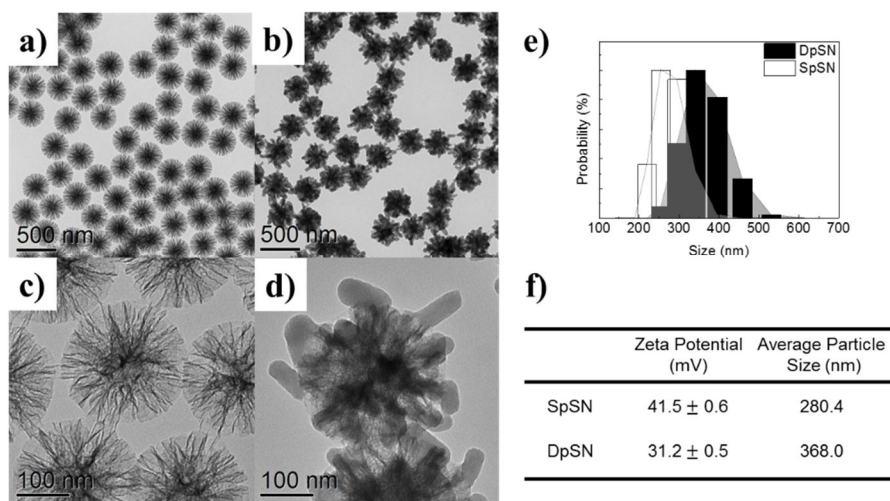


**Figure 2.1.** Characterization of synthesized SpSN and DpSN. Transmission electron microscope (TEM) images of (a), (c) SpSN and (b), (d) DpSN. (e) Dynamic light scattering (DLS) measurement exhibited increased hydrodynamic diameter of DpSN from the formation of branched nanostructures. (f)  $\zeta$ -potential and average particle diameter from DLS measurement of SpSN and DpSN.

	Pore size (nm)	BET surface area (m <sup>2</sup> g <sup>-1</sup> )	Pore volume (mL g <sup>-1</sup> )
SpSN	45.9 nm	581.55	2.00
Branched part	~ 3 nm	780.96	1.02
DpSN	~ 3 nm, 43. 7 nm	558.98	1.20

**Table 2.1.** N<sub>2</sub> adsorption/desorption data of SpSN, DpSN and separately prepared Branched part of DpSN was summarized.

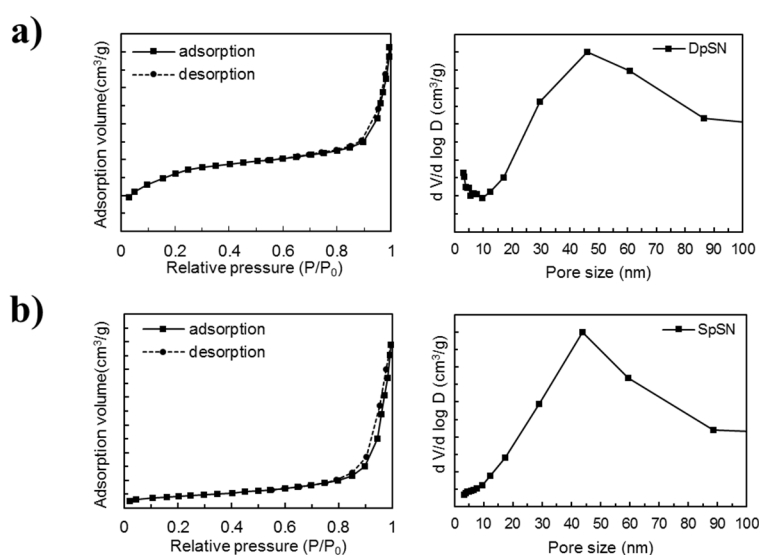


**Figure 2.2.** N<sub>2</sub> adsorption/desorption for characterization of pore size by Brunauer-Emmett-Teller (BET) method. Measured type-IV isotherm curves of adsorption volume (left) and calculated pore size distribution (right) of (a) DpSN and b) SpSN was represented.

VW growth, which played a key role in the formation of the present DpSN, is commonly used to construct Janus nanostructures. The driving force of scintillating nanostructure formation was dominantly governed by surface energy difference of components, as represented by equation (1) :

$$\Delta\sigma = \sigma_{branch-solvent} + \sigma_{branch-SpSN \text{ interface}} - \sigma_{SpSN-solvent} \quad (1)$$

where  $\sigma_{SpSN-solvent}$  and  $\sigma_{branch-solvent}$  respectively represented the surface energy from the interface of SpSN and branched nanostructure with adjacent solvent molecules, and  $\sigma_{branch-SpSN \text{ interface}}$  represented the interface energy between growth template SpSN and newly formed branched nanostructures. Previous reports suggested that the positive surface energy difference ( $\Delta\sigma > 0$ ) induced the VW growth pathway as branched nanostructure formation on the template nanostructure, and negative surface energy difference ( $\Delta\sigma < 0$ ) resulted core-shell nanostructure formation by Frank-van der Merwe growth pathway.<sup>[10]</sup> Therefore, the formation of DpSN could be accomplished when sum of  $\sigma_{branch-solvent}$  and  $\sigma_{branch-SpSN \text{ interface}}$  is larger than  $\sigma_{SpSN-solvent}$  by dominant VW growth pathway.



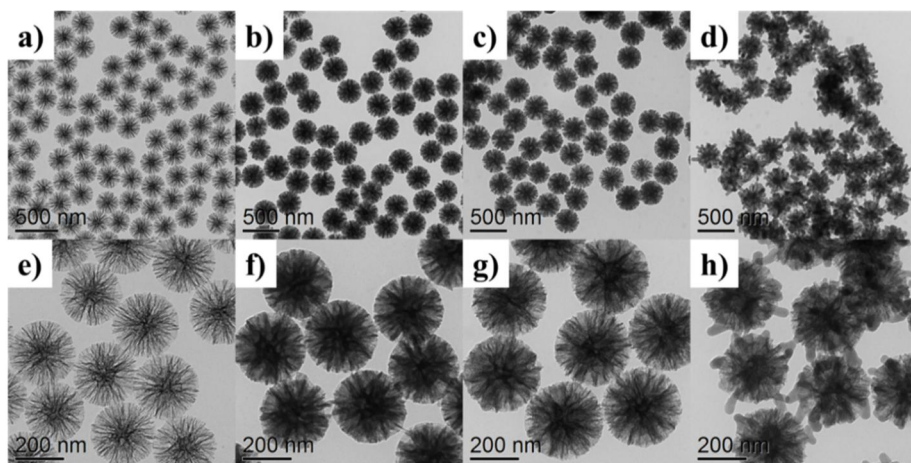


**Figure 2.3.** Difference in secondary silica nanostructure formation against the surface moiety and existence of trisodium citrate additive. TEM images of (a) SpSN without surface functionalization and secondary nanostructure developed on (b) propyl-grafted SpSN, aminopropyl-grafted SpSN (c) without trisodium citrate, and (d) with trisodium citrate additive. The images (e-h) at bottom implied higher magnification TEM images of (a-d), respectively

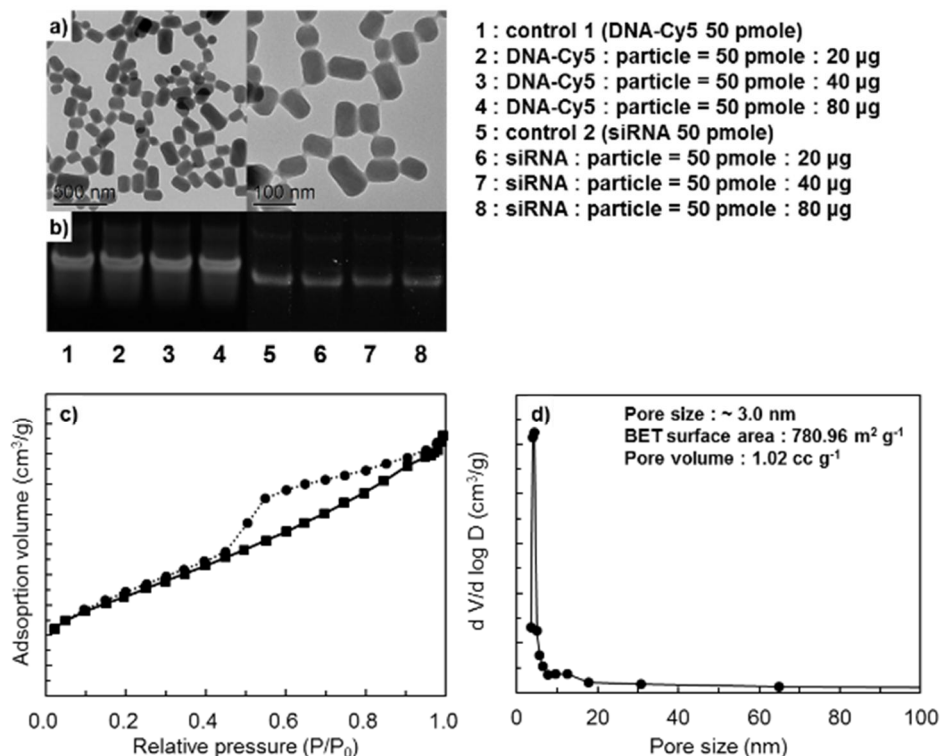


**Figure 2.4.** Characterization of the separately synthesized branched part of DpSN. a) low and high magnification images of the branched particle. b) the loading capacity of branched silica subunit nanoparticle against oligonucleotide (DNA-Cy5 and siRNA) was confirmed by gel-electrophoresis. c) isotherm curves, and d) the distribution of pore size data.

To confirm the mechanism of DpSN formation, we performed secondary silica nanostructure growth under the additive control. In order to lower the  $\sigma_{\text{SpSN-solvent}}$  value, hydrophobic SpSN surface should become hydrophilic under the basic condition.<sup>[19,20]</sup> We additionally treated trisodium citrate as an acidic additive to maintain the surface hydrophilicity of SpSN during secondary silica nanostructure growth for protonation of introduced aminopropyl functional groups of SpSN surface.<sup>[21]</sup> According to the TEM observation, addition of trisodium citrate successfully induced the VW growth pathway due to positive  $\Delta\sigma$  by reducing  $\sigma_{\text{SpSN-solvent}}$  against aminopropyl-grafted SpSN compared to propyl-grafted SpSN where protonation could not occur. **(Figure 2.3)**

In order to confirm the presence of dual-sized pores and calculation of respective values, we performed nitrogen adsorption/desorption measurement against prepared SpSN and DpSN. It was confirmed that the existence of pores having a diameter of 2-3 nm was observed simultaneously in the DpSN (BET surface area: 558.98 m<sup>2</sup> g<sup>-1</sup>, pore volume: 1.20 mL g<sup>-1</sup>), while the SpSN (BET surface area: 581.55 m<sup>2</sup> g<sup>-1</sup>, pore volume: 2.00 mL g<sup>-1</sup>) only exhibited the presence of pores with a diameter of 40-45 nm range. **(Figure 2.2 and Table 2.1)** Also, to validate source of small pore in DpSN, the branched part without the SpSN was synthesized, and the presence of small pore of the branched part (2-3 nm) was verified by nitrogen adsorption/desorption. **(Figure 2.4a,c,d).**

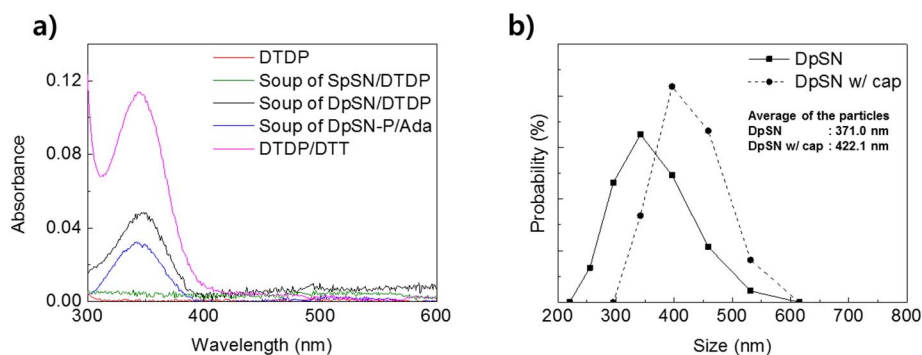


**Figure 2.5.** Characterization of conjugation of 1-adamantanethiol. a) UV-Vis spectrum; DTDP = 2,2'-dithiodipyridine solution, DpSN-P = 2-pyridinethiol conjugated DpSN, and Ada = 1-adamantanethiol solution. b) Size distribution of the particles.

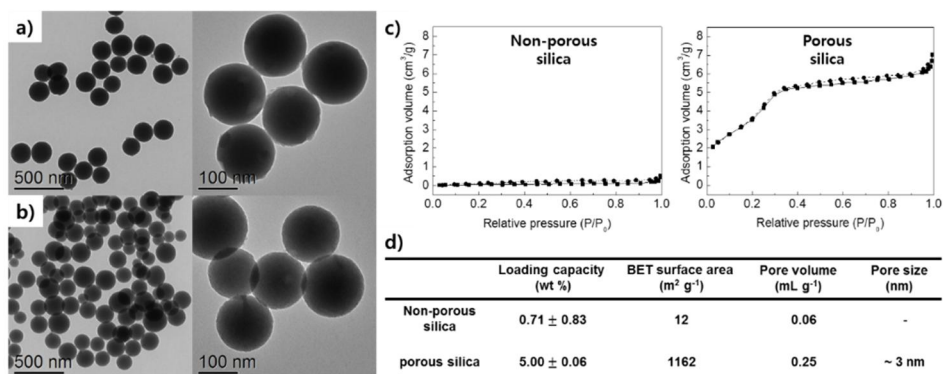


**Figure 2.6.** Characterization of synthesized porous silica nanoparticles and non-porous silica nanoparticles. TEM images of a) non-porous silica nanoparticles and b) porous silica nanoparticles in low and high magnification, c) N<sub>2</sub> adsorption/desorption data plotting, and d) table of the information about silica nanoparticles depending on the presence or absence of porosity.

From this observation, we concluded that synthesized DpSN by VW growth method contains dual-pore hetero-system of larger (40-45 nm, core) and smaller (2-3 nm, branch) pores for sufficient loading of relatively bulky oligonucleotides and small drug molecules, respectively. Furthermore, aminopropyl modified core and mercaptopropyl modified branch domains of DpSN endowed efficient dual cargo delivering feasibility. Positively charged large pored core domain would enable negatively charged oligonucleotide payload by electrostatic interaction, and following controlled release by *in vitro* anion exchange.<sup>[22]</sup> Smaller pored branch domain was appropriate for diffusive loading of small drug molecules, and existence of thiol functional groups would allow the additional introduction of pore capping strategy for controlled release by disulfide bond chemistry.<sup>[23,24]</sup> (**Scheme 2.1**)

To confirm the dual cargo loading and release capability, we performed the model compound loading for Cy5-DNA and Rho 6G to core and branch domain, respectively. To prevent the outflow of diffusively loaded Rho 6G into branch domain pore, disulfide bond mediated additional functionalization with 1-adamantanethiol and following  $\beta$ -cyclodextrin capping were carried out. To validate the capping on DpSN, firstly, disulfide bond between thiol group in DpSN and 2-pyridinethiol was observed through detecting the peak of 350 nm induced by 4-thiopyridine (TPD), because TPD was formed via reaction between thio group and 2,2'-dithiodipyridine (DTDP).<sup>[25,26]</sup> The peak of 350 nm was detected in soup of solution containing DTDP and DpSN, which indicate

the disulfide bond was formed in only DpSN containing thiol group. (**Figure 2.5a**) Then, to make disulfide bond between 1-adamantanethiol and DpSN, above sample was washed and re-dispersed in solution containing 1-adamantanethiol. The peak of 350 nm was observable again in soup of the above solution because TPD was re-formed via thiol-disulfide exchange between 1-adamantanethiol and 2-pyridinethiol conjugated-DpSN.<sup>[27]</sup> (**Figure 2.5a**) As a result, it could be deducible that disulfide bond between 1-adamantanethiol and DpSN was formed. Additionally, the shift of size distribution was observed by DLS, resulting in presence of capping. (**Figure 2.5b**)

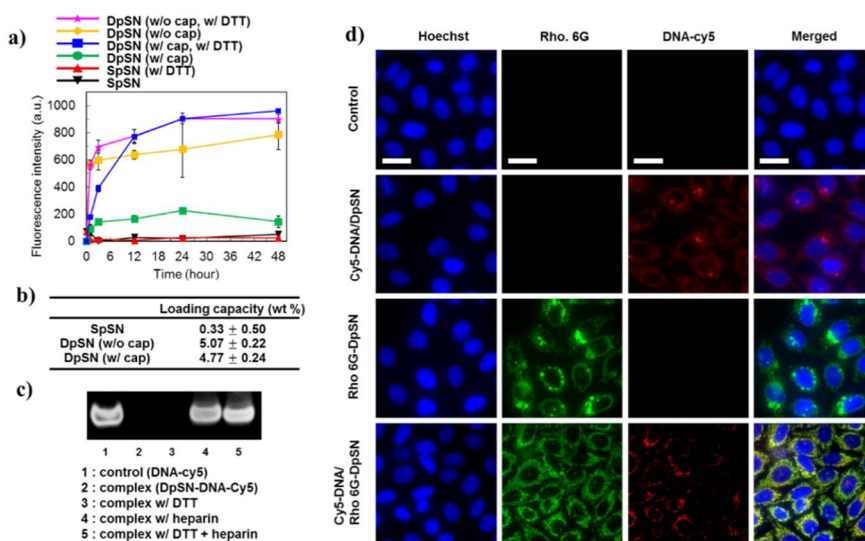


**Figure 2.7.** Loading and release profile of Cy5-DNA and Rho 6G as model cargos for SpSN and DpSN. (a) Release kinetics of the loaded Rho 6G was measured in 1X PBS solution in the presence of 10 mM dithiothreitol (DTT). (b) Loading capacities were calculated for SpSN and DpSN. (c) Loading capacity of Cy5-DNA was evaluated by polyacrylamide gel electrophoresis (PAGE). (d) Confocal laser scanning microscope (CLSM) images of Cy5-DNA and/or Rho 6G loaded DpSN treated HeLa cells. Cell nuclei were stained with Hoechst 33342 (blue) before microscope observation. Scale bar is 25  $\mu$ m.

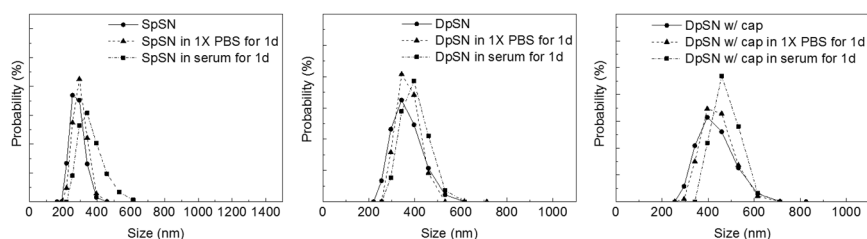


**Figure 2.8.** The colloidal stability of the SpSN, DpSN, and DpSN with capping was characterized by DLS measurement against 1 d incubation in 1x PBS and serum containing media.

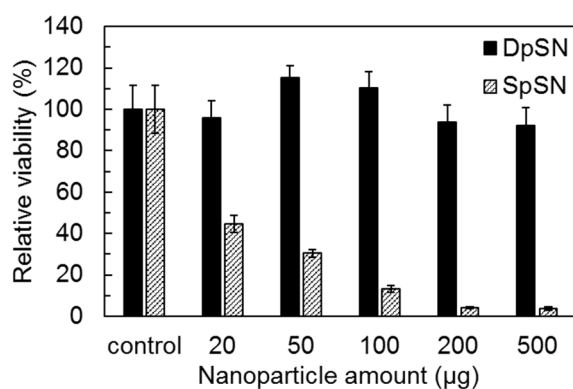


**Figure 2.9.** Cytotoxicity of DpSN and SpSN was evaluated by MTT assay.

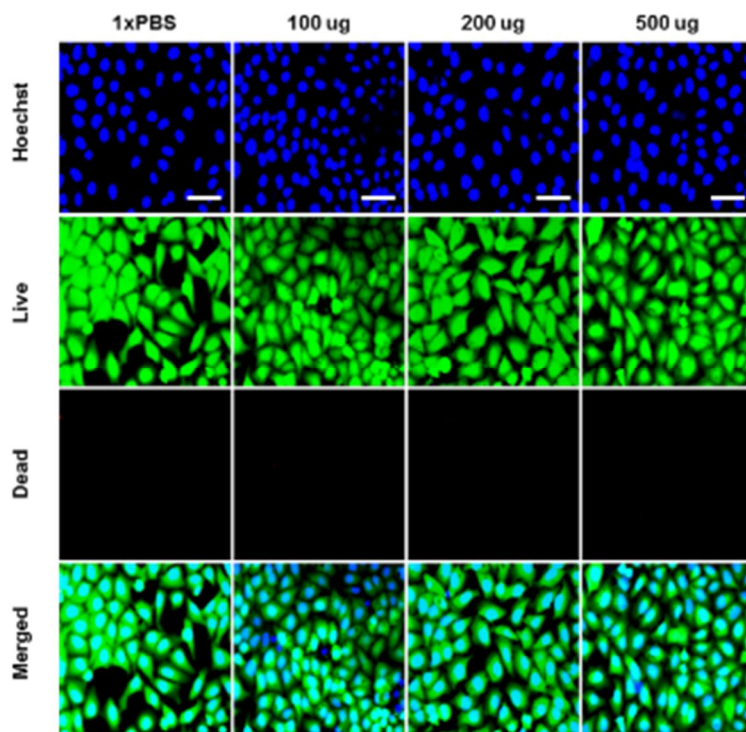


**Figure 2.10.** Fluorescent images of DpSN treated HeLa cells with Hoechst 33342 (Nuclei, blue), Calcein AM (Live, green), and EthD-1 (Dead, red) staining. Scale bar is 50 mm.



Calculated loading capacity of Rho 6G of DpSN was significantly higher than that of SpSN by 15.4 times (w/o capping) and 14.5 times (w/ capping). (**Figure 2.7b**) Additionally, to verify that the drugs were loaded into the pore, the loading capacity of the porous silica was compared with that of the non-porous silica. The silica nanoparticles, used in studying pore effect for loading capacity, had similar size and morphology, but only difference of the existence of pore. (**Figure 2.6a,b**) The loading capacity of porous silica was  $5.00 \pm 0.06$  wt%, while that of non-porous silica was  $0.71 \pm 0.83$  wt%, which was negligible and unreliable in error range. Therefore, it was deduced that small molecule was loaded into the pore in porous silica nanoparticle. Controlled release of Rho 6G by capping strategy was also clearly verified by fluorescence intensity measurement of Rho 6G (at 555 nm). Without capping, the loaded Rho 6G onto DpSN exhibited burst release within 3 hr with unreproducible value, while capping guaranteed almost perfect and controlled release kinetics ( $96.1 \pm 1.2$  % and  $14.5 \pm 4.2$  % at 48 hr incubation w/ and w/o dithiothreitol treatment, respectively). (**Figure 2.7a**) Also, loading capacity of Cy5-DNA into core domain was calculated as 1.25 pmol DNA/ $\mu$ g DpSN, (**Figure 2.12a**) which was not notably changed by Rho 6G loading in branch domain. Also, loading capacity of oligonucleotide was only affected by the positively charged core part, but not the branched part because its loading capacity of oligonucleotide was negligible. (**Figure 2.4b**) Loading and release of Cy5-DNA was confirmed by gel electrophoresis. (**Figure 2.7c**) In vitro

release of Cy5-DNA ( $\lambda_{\text{ex}}=650$  nm and  $\lambda_{\text{em}}=670$  nm) and Rho 6G ( $\lambda_{\text{ex}}=528$  nm and  $\lambda_{\text{em}}=555$  nm) was characterized by confocal scanning laser microscopy (CSLM) using HeLa cells. According to the fluorescence images, mono- or dual-cargo delivery was clearly confirmed by the corresponding fluorescence in cytoplasmic region. (**Figure 2.7d**) While Cy5-DNA fluorescence signals were detected in both SpSN and DpSN, Rho 6G was observed only in DpSN, which additionally supported the desired drug loading and delivery *via* hybrid nanoparticle with different surface environments and pore size. (**Figure 2.13**)

Loading of charged cargoes, such as negatively charged oligonucleotide, would induce the fluctuation of  $\zeta$ -potential. To study this phenomenon,  $\zeta$ -potential was estimated against SpSN and DpSN with oligonucleotide and Dox. According to the measurement, as we expected, Dox loading did not involve a change in the zeta potential, while the loading of oligonucleotides could confirm the phenomenon of lowering the zeta potential. (**Table 2.2**) Compared with the bare carriers, the zeta potential of cargo loaded-carriers had lower value, due to negatively charged cargo, such as nucleic acids.<sup>[28]</sup>

Colloidal stability of DpSN, DpSN with capping and SpSN was estimated by DLS along with incubation for 1 day in physiological buffered solution 1x PBS and serum containing media. There was no significant changes in size distribution, indicated that the used particles were stable in the buffer and the serum condition. (**Figure 2.8**) Next, we measured cytotoxicity of the

synthesized SpSN and DpSN in HeLa cell line by using MTT cell viability assay. Compared to untreated cells as control, DpSN exhibited very high cell viability up to 500  $\mu\text{g}$  of nanoparticle treatment ( $92.0 \pm 8.7$  % viable), (**Figure 2.9** and **2.10**) whereas SpSN represented dose-dependent cytotoxicity ( $3.7 \pm 0.7$  % viable against 500  $\mu\text{g}$  treatment). (**Figure 2.9**)

Nanomaterials in a cell would cause damage of membrane, protein, nucleic acid, resulting in cytotoxicity,<sup>[29]</sup> and there were a lot of factors related to the cytotoxicity of nanoparticle in cell, such as surface charge, cellular uptake, size, aggregation, and, morphology of the particles.<sup>[30]</sup> In Addition, each factors would be inter-connected and showed different effects on case by case. For example, efficiency of the uptake of the particles was differently affected by the symmetry of the particles.<sup>[31,32]</sup> Therefore, cytotoxic effects of nanoparticle needed to be evaluate carefully. In case of SpSN, Non-aminated SpSN ( $-17.77 \pm 1.60$  mV,  $57.6 \pm 2.5$  % viable against 500  $\mu\text{g}$  treatment) with the same morphology of SpSN represented less cytotoxicity in HeLa cell than SpSN ( $41.5 \pm 0.6$  mV,  $3.7 \pm 0.7$  % viable against 500  $\mu\text{g}$  treatment). (**Figure 2.11**) As a result, surface charge seemed to affect to cell viability rather than morphological effect in this case,<sup>[33,34]</sup> but various factors, such as formation of protein corona and agglomeration, should be considered.<sup>[30]</sup>

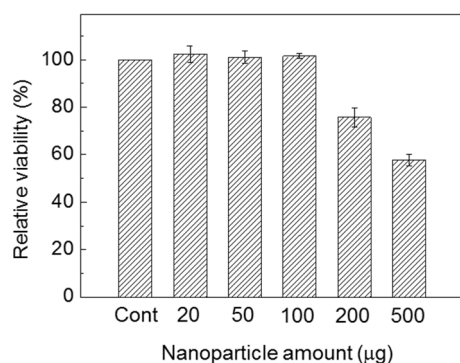


**Figure 2.11.** Cytotoxicity of non-aminated SpSN was evaluated by MTT assay.

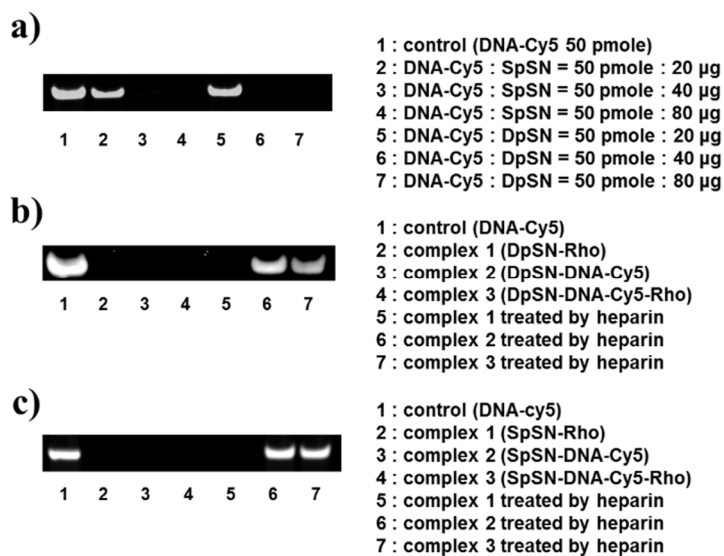


**Figure 2.12.** Cy5-DNA loading capacity and release profile of SpSN and DpSN were calculated by PAGE. (a) loading capacity of Cy5-DNA towards SpSN and DpSN. Release profile of Cy5-DNA and/or Rho 6G from (b) DpSN and (c) SpSN.

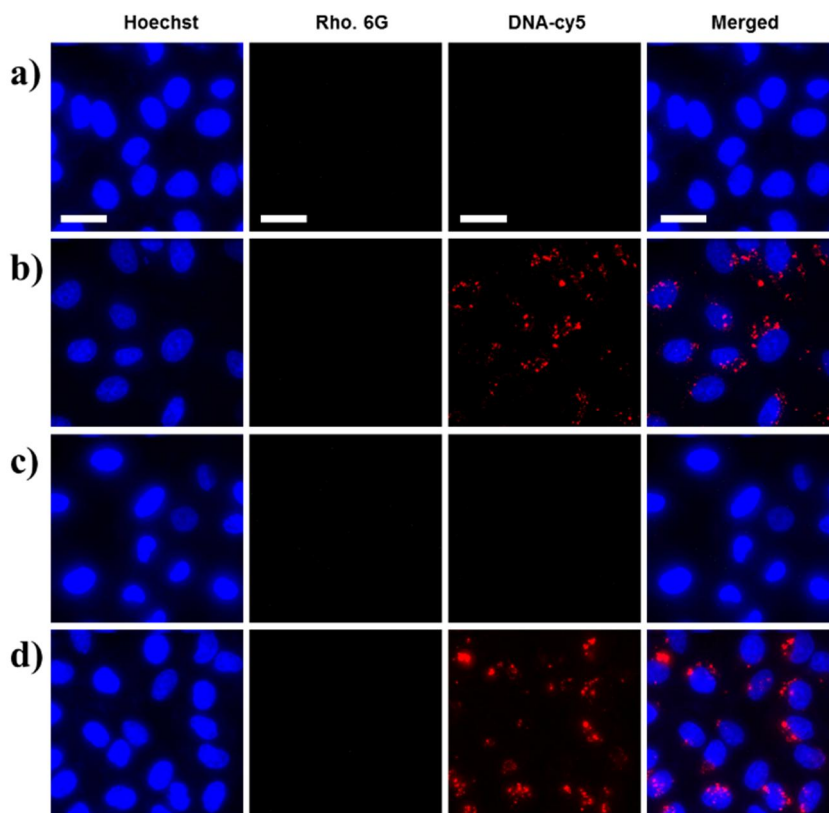


**Figure 2.13.** The fluorescence microscope images of Cy5-DNA and/or Rho 6G loaded SpSN. It showed that SpSN could not exhibit the delivering capability against Cy5-DNA. ; a) control, b) DNA-Cy5 + SpSN complex, c) Rho. 6G + SpSN complex, and d) Rho. 6G + DNA Cy-5 + SpSN complex. The scale bar is 25  $\mu\text{m}$ .

	Zeta potential (mV)		Zeta potential (mV)
SpSN	$41.5 \pm 0.6$	DpSN	$31.2 \pm 0.5$
SpSN-DNA-Cy5	$17.5 \pm 0.6$	DpSN-DNA-Cy5	$17.2 \pm 0.3$
SpSN-siBcl-2	$16.3 \pm 0.8$	DpSN-DOX	$32.1 \pm 1.3$
		DpSN-siBcl-2	$16.6 \pm 0.2$
		DpSN-siBcl-2-DOX	$17.0 \pm 0.0$

**Table 2.2.** Zeta-potential of SpNP and DpSN against the loading of cargos.

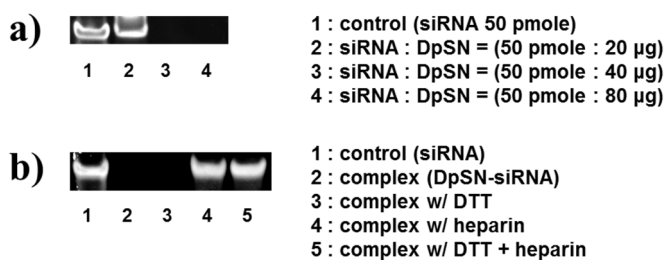


**Figure 2.14.** (a) Loading capacity and (b) releasing behavior of siRNA under various conditions were estimated by PAGE.

Prior to the therapeutic efficacy measurement, we performed the therapeutic efficiency of free Dox treatment with varying the concentration. According to the MTT assay, no distinctive therapeutic effect was exhibited below 50 pmol of free Dox treatment against 24 and 48 hr of treatment. From the 100 pmol of free Dox treated condition, cell viability decrease was observed in dose-dependent manner. **(Figure 2.15)** Then, we performed additional characterizations to secure solid evidences of siRNA delivery and knockdown efficiency. By using 6-carboxylfluorescein (FAM) conjugated DpSN and Cy5 fluorescently labelled siRNA (Cy5-siRNA), fluorescence signal superposition was tracked over the incubation time. **(Figure 2.16 and 2.17)** From the statistical processing, we successfully showed the release of loaded siRNA through the decrease of Pearson's correlation coefficient of detected fluorescence signal overlapping.<sup>[35]</sup> Target gene knockdown by the released siRNA was evaluated using green fluorescence protein (GFP) transfected HeLa cells and siRNA against GFP (siGFP) through fluorescence microscopy and fluorescence-activated cell sorting (FACS) analysis. Compared to siGFP delivery by using widely used conventional transfecting agent, lipofectamine, DpSN mediated siRNA delivery represented slightly higher knockdown efficiency. **(Figure 2.18 and 2.19)**

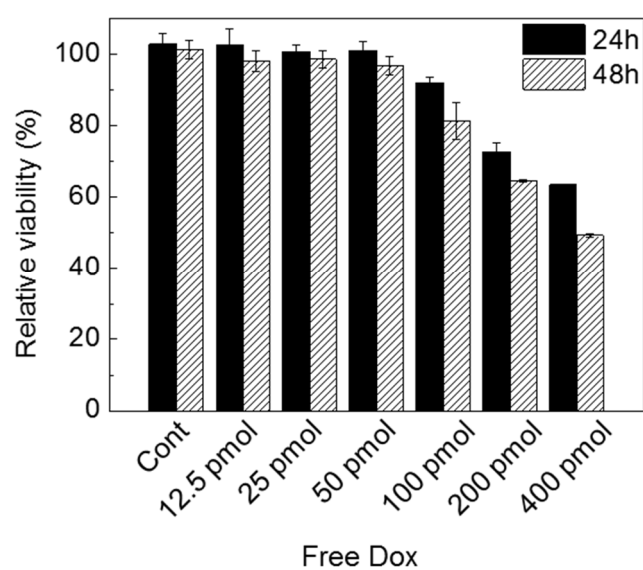


**Figure 2.15.** MTT cell viability assay against free Dox treatment in various concentrations.



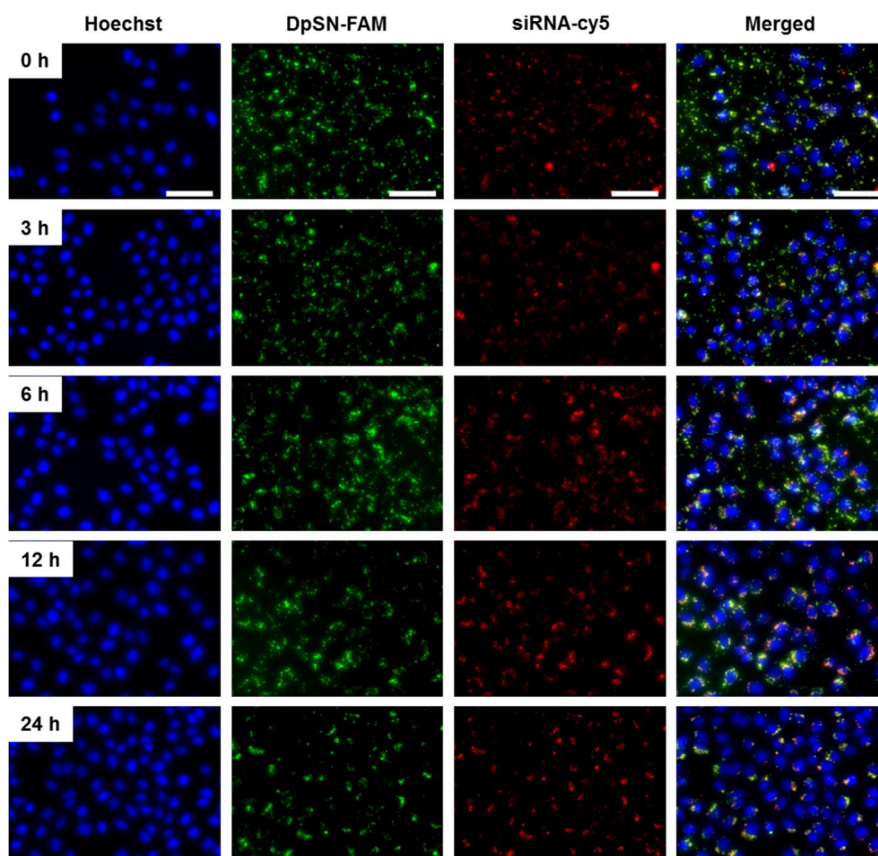


**Figure 2.16.** Time-dependent release of Cy5-siRNA from FAM-DpSN was observed inside cells. The Cy5-siRNA loaded FAM-DpSN was shown as yellowish color by fluorescence signal superposition, and it gradually decreased over time due to Cy5-siRNA release (red) from FAM-DpSN (green). The scale bar is 100  $\mu\text{m}$ .

Pearson's correlation coefficient		
	DpSN-siRNA	DpSN-siRNA-DOX
0	0.767	0.797
3	0.732	0.732
6	0.727	0.715
12	0.699	0.689
24	0.697	0.677

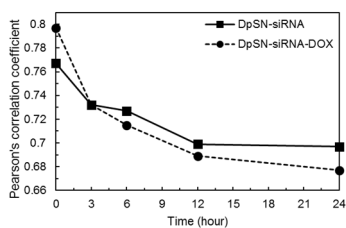


**Figure 2.17.** Pearson's correlation coefficient which indicates the overlapping area between FAM-DpSN and Cy5-siRNA was calculated. Pearson's correlation coefficient "1" indicates perfect overlap.

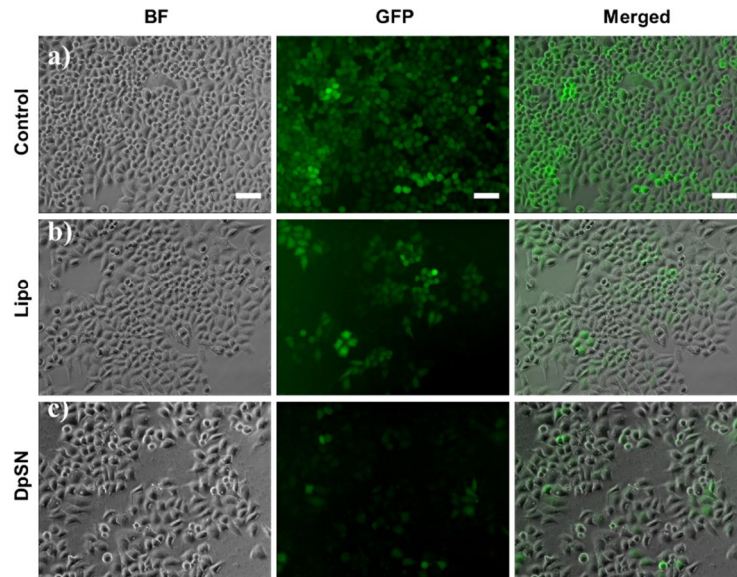


**Figure 2.18.** Fluorescent images of GFP expression in GFP-HeLa cells. (a) control, (b) siGFP + lipofectamine complex, and (c) siGFP + DpSN. The scale bar is 100  $\mu\text{m}$ .

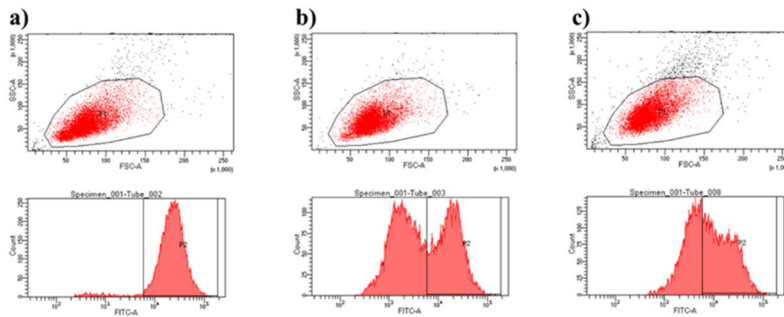


**Figure 2.19.** Knockdown efficiency of GFP induced by siGFP was estimated by FACS. (a) control, (b) siGFP + lipofectamine complex, and (c) siGFP + DpSN. DpSN was more efficient in inducing GFP knockdown by siGFP than lipofectamine as a delivery carrier.

Finally, the combinational gene-chemo cancer therapeutic efficacy was quantitatively studied by using siBcl-2 and Dox against HeLa cell line.<sup>[2,36]</sup> Compared to the negligible therapeutic efficiency of free siBcl-2 ( $96.9 \pm 6.0\%$  and  $100.0 \pm 1.0\%$ ), free Dox ( $96.6 \pm 14.5\%$  and  $99.6 \pm 3.7\%$ ), dual treatment of free siBcl-2/Dox ( $90.2 \pm 14.5\%$  and  $99.0 \pm 2.2\%$ ), and moderate mono-modal treatment of siBcl-2 ( $79.2 \pm 1.9\%$  and  $33.5 \pm 1.0\%$ ) or Dox ( $64.4 \pm 0.6\%$  and  $39.4 \pm 2.5\%$ ) through DpSN, gene-chemo combinational treatment using DpSN clearly exhibited significantly higher therapeutic efficacy in all cases of 24 and 48 hr treatment ( $31.1 \pm 2.7\%$  and  $16.6 \pm 1.9\%$  viable at 24 and 48 hr incubation, respectively). (**Figure 2.20a**) The projected additives were calculated from the multiply of each survivor rate of single treatment in order to confirm the synergistic effect of dual-therapy.<sup>[37]</sup> Because the projected additive was calculated from the multiply of each survivor rate, the results of 48 hr showed a reduced value compared to 24 hr. Also, the difference between survivor rate of dual-therapy and the projective additives reduced with increasing time, which can be interpreted as representing less efficient synergistic anti-cancer effect with increasing dual-drug DpSN nanocomplex treatment time at this experimental condition. Reverse transcription polymerase chain reaction (RT-PCR) also proved that the DpSN mediated siBcl-2 delivery induced the knockdown of Bcl-2 gene. (**Figure 2.20b**) Additionally, live/dead staining by Calcein AM (green) and EhiD-1 (red) followed by fluorescence microscope observation and the analysis of fluorescence images with ImageJ

provided further evidence of the effectiveness of gene-chemo combinational cancer therapy by using DpSN as versatile delivery carrier.<sup>[38,39]</sup> (**Figure 2.20c** and **Figure 2.21**)

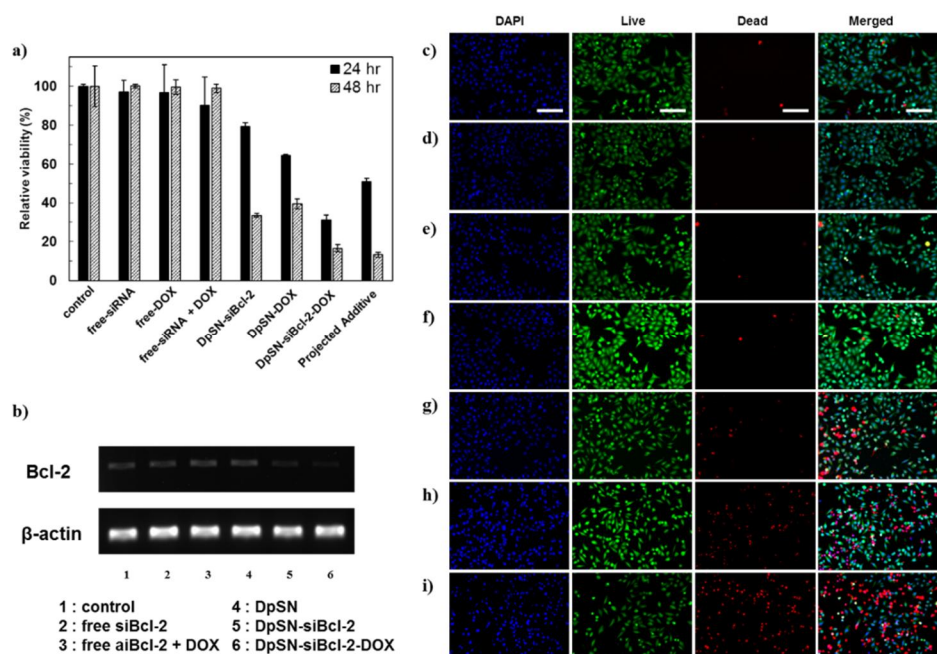


**Figure 2.20.** The quantitative therapeutic efficiency comparison. (a) MTT cell viability assay of free cargos, mono-modal therapy, and dual-modal gene-chemo combinational therapy at 24 and 48 hr incubation against untreated cells (denoted as control). (b) Knockdown efficiency of Bcl-2 gene was validated by using RT-PCR with  $\beta$ -actin as housekeeping gene. (c) Fluorescent microscope images of live/dead stained HeLa cells. Nuclei (DAPI, blue), live cells (Calcein AM, green) and dead cells (EthiD-1, red) fluorescence signals and merged images exhibited combinational therapeutic efficiency. Scale bar is 200  $\mu$ m.

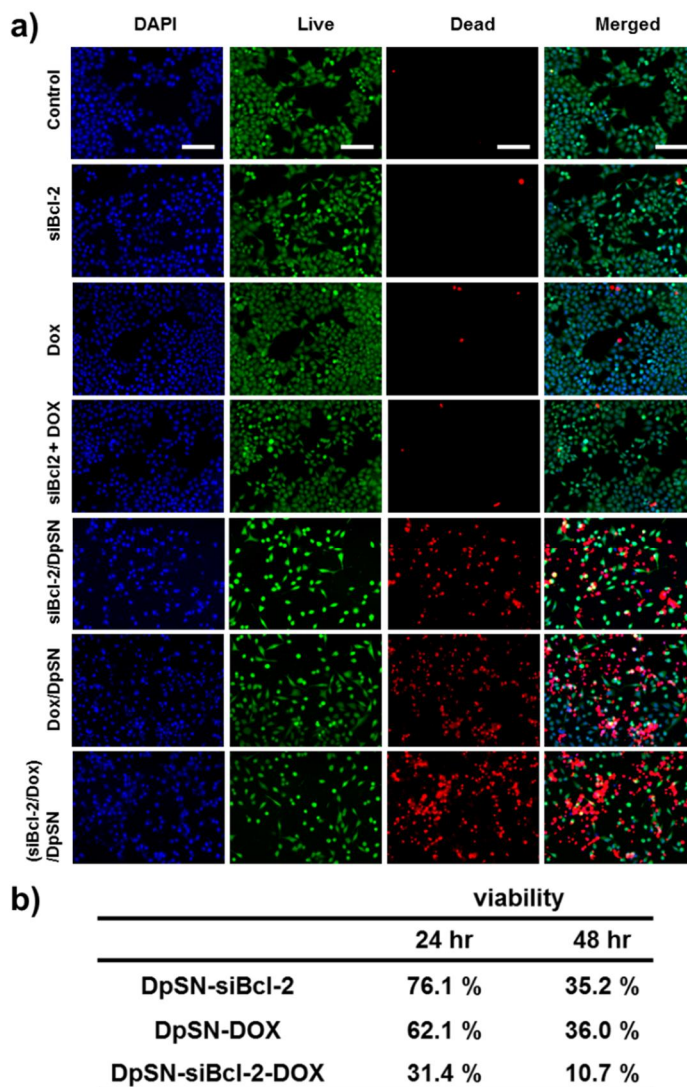


**Figure 2.21.** Live/dead staining mediated fluorescent images against gene or/and chemo treated cells. a) the Fluorescent images of the cell after 48 hr from treatment; Nuclei (DAPI, blue), live cells (Calcein AM, green) and dead cells (EthiD-1, red). Scale bar is 200  $\mu$ m. b) Quantitatively analyzed cell viability by using ImageJ program.

## **2. 4. Conclusion**

In conclusion, we successfully developed dual-sized pore containing hybrid porous silica nanoparticle by surface energy difference controlled synthetic procedure. Manufactured nanoparticle exhibited coexistence of large (40-45 nm) and small (2-3 nm) pores in their core and branch domain with distinctive surface functional groups for multiple strategic cargo loading. Present DpSN platform represented highly efficient loading and controlled release feature of siRNA and anticancer chemical drug from each appropriate nanostructure. Considering the efficacy in drug delivery and excellent biocompatibility, DpSN is believed to be regarded as a promising nanoparticle for various biomedical applications.



## 2. 5. References

- [1] M. R. Stratton, P. J. Cambell, P. A. Futreal, *Nature* **2009**, *458*, 719-724.
- [2] M. Saraswathy, S. Gong, *Mater. Today* **2014**, *17*, 298-306.
- [3] H. Xie, Z. G. She, S. Wang, G. Sharma, J. W. Smith, *Langmuir* **2012**, *28*, 4459-4463.
- [4] W. Xu, P. A. Ledin, Z. Iatridi, C. Tsitsilianis, V. V. Tsukruk, *Angew. Chem. Int. Ed.* **2016**, *55*, 4908-4913.
- [5] C. Xu, J. Xie, D. Ho, C. Wang, N. Kohler, E. G. Walsh, J. R. Morgan, Y. E. Chin, S. Sun, *Angew. Chem. Int. Ed.* **2008**, *47*, 173-176.
- [6] I. Schick, S. Lorenz, D. Gehrig, A. M. Schilmann, H. Bauer, M. Panthöfer, K. Fischer, D. Strand, F. Laquai, W. Tremel, *J. Am. Chem. Soc.* **2014**, *136*, 2473-2483.
- [7] Y. Liu, X. Yang, Z. Huang, P. Huang, Y. Zhang, L. Deng, Z. Wang, Z. Zhou, Y. Liu, H. Kalish, N. M. Khachab, X. Chen, Z. Nie, *Angew. Chem. Int. Ed.* **2016**, *55*, 15297-15300.
- [8] L. Zhang, Y. Chen, Z. Li, L. Li, S. C. Philippe, C. Li, J. Lin, X. Wang, Z. Su, J. I. Zink, *Angew. Chem. Int. Ed.* **2016**, *55*, 2118-2121.
- [9] P. J. Chen, Y. D. Kang, C. H. Lin, S. Y. Chen, C. H. Hsieh, Y. Y. Chen, C. W. Chiang, W. Lee, C. Y. Hsu, L. D. Liao, C. T. Fan, M. L. Li, W. C. Shyu, *Adv. Mater.* **2015**, *27*, 6488-6495.
- [10] X. Li, L. Zhou, Y. Wei, A. M. El-Toni, F. Zhang, D. Zhao, *J. Am. Chem. Soc.* **2014**, *136*, 15086-15092.

- [11] K. Lee, Y. Yi, Y. Yu, *Angew. Chem. Int. Ed.* **2016**, *55*, 7384-7387.
- [12] H. Meng, W. X. Mai, H. Zhang, M. Xue, T. Xia, S. Lin, X. Wang, Y. Zhao, Z. Ji, J. I. Zink, A. E. Nel, *ACS Nano* **2013**, *7*, 994-1005.
- [13] Y. Wang, S. Gao, W. H. Ye, H. S. Yoon, Y. Y. Yang, *Nat. Mater.* **2006**, *5*, 791-796.
- [14] J. Conde, N. Oliva, Y. Zhang, N. Artzi, *Nat. Mater.* **2016**, *15*, 1128-1138.
- [15] Y. Feng, J. He, H. Wang, Y. Y. Tay, H. Sun, L. Zhu, H. Chen, *J. Am. Chem. Soc.* **2012**, *134*, 2004-2007.
- [16] S. G. Kwon, G. Krylova, P. J. Phillips, R. F. Klie, S. Chattopadhyay, T. Shibata, E. E. Bunel, Y. Liu, V. B. Prakapenka, B. Lee, E. V. Shevchenko, *Nat. Mater.* **2015**, *14*, 215-223.
- [17] J. Croissant, X. Cattoën, M. W. C. Man, P. Diedonné, C. Charnay, L. Raehm, J. O. Durand, *Adv. Mater.* **2015**, *27*, 145-149.
- [18] V. Polshettiwar, D. Cha, X. Zhang, J. M. Basset, *Angew. Chem. Int. Ed.* **2010**, *49*, 9652-9656.
- [19] T. Suteewong, H. Sai, M. Bradbury, L. A. Estroff, S. M. Gruner, U. Wiesner, *Chem. Mater.* **2012**, *24*, 3895-3905.
- [20] R. Atluri, Y. Sakamoto, A. E. Garcia-Bennett, *Langmuir* **2009**, *14*, 3189-3195.
- [21] T. Suteewong, H. Sai, R. Hovden, D. Muller, M. S. Bradbury, S. M. Gruner, U. Wiesner, *Science* **2013**, *340*, 337-341.

- [22] H. K. Na, M. H. Kim, K. Park, S. R. Ryoo, K. E. Lee, H. Jeon, R. Ryoo, C. Hyeon, D. H. Min, *small* **2012**, 8, 1752-1761.
- [23] J. Lai, B. P. Shah, E. Garfunkel, K. B. Lee, *ACS Nano* **2013**, 7, 2741-2750.
- [24] C. Y. Lai, B. G. Trewyn, D. M. Jeftinija, K. Jeftinija, S. Xu, S. Jeftinija, V. S. Y. Lin, *J. Am. Chem. Soc.* **2003**, 125, 4451-4459.
- [25] H. Chen, H. Zou, H. J. Paholak, M. Ito, W. Qian, Y. Che, D. Sun, *Polym. Chem.* **2014**, 5, 2768-2773.
- [26] M. Moser, T. Behnke, C. Hamers-Allin, K. K-Hartwig, J. Falkenhagen, U. Resch-Genger, *Anal. Chem.* **2016**, 88, 8624-8631.
- [27] J. R. Winther, C. Thorpe, *Biochim. Biophys. Acta* **2014**, 1840, 838-846.
- [28] C. Tao, Y. Zhu, X. Li, N. Hanagata, *RSC Adv.* **2014**, 4, 45823-45830.
- [29] P. P. Fu, Q. Xia, H. M. Hwang, P. C. Ray, H. Yu, *J. Food Drug Anal.* 2014, 22, 64-75.
- [30] S. J. Seo, M. Chen, H. Wang, M. S. Kang, K. W. Leong, H. W. Kim, *Nano Today* 2017, 14, 84-99.
- [31] S. E. A. Gratton, P. A. Ropp, P. D. Pohlhaus, J. C. Luft, V. J. Madden, M. E. Napier, J. M. DeSimone, *Proc. Natl. Acad. Sci. U.S.A.* 2008, 105, 11613-11618.
- [32] B. D. Chithrani, A. A. Ghazani, W. C. W. Chan, *Nano Lett.* 2006, 6, 662-668.
- [33] E. Fröhlich, *Int. J. Nanomed.* **2012**, 7, 5577-5591.
- [34] C. Hoskins, A. Cuschieri, L. Wang, *J. Nanobiotechnol.* 2012, 10, 15.
- [35] J. Adler, I. Parmryd, *Cytom. Part A* **2010**, 77, 733-742.

- [36] U. Akar, A. Chaves-Reyes, M. Barria, A. Tari, A. Sanguino, Y. Kondo, S. Kondo, B. Arun, G. Lopez-Berestein, B. Ozpolat, *Autophagy* **2008**, 4, 669-679.
- [37] T. S. Hauck, T. L. Jennings, T. Yassenko, J. C. Kumaradas, W. C. W. Chan, *Adv. Mater.* **2008**, 20, 3832-3838.
- [38] B. Duan, L. A. Hockaday, K. H. Kang, J. T. Butcher, *J. Biomed. Mater. Res. A* **2013**, 101A, 1255-1264.
- [39] D. S. W. Benoit, M. C. Tripodi, J. O. Blanchette, S. J. Langer, L. A. Leinwand, K. S. Anseth, *J. Biomed. Mater. Res. A* **2007**, 81A, 259-268.
- [40] D. S. Moon, J. K. Lee, *Langmuir* **2012**, 28, 12341-12347.
- [41] J. Lai, B. P. Shah, E. Garfunkel, K. B. Lee, *ACS Nano* **2013**, 7, 2741-2750.
- [42] S. Kim, H. K. Na, C. Won, D. H. Min, *RSC Adv.* **2016**, 6, 27143-27150.
- [43] M. H. Kim, H. K. Na, Y. K. Kim, S. R. Ryoo, H. S. Cho, K. E. Lee, H. Jeon, R. Ryoo, D. H. Min, *ACS Nano* **2011**, 5, 3568-3576.
- [44] I. A. M. Ibrahim, A. A. F. Zikry, M. A. Sharaf, *J. Am. Sci.* **2010**, 6, 985-989

# **Chapter 3. Graphene-Masked Selective Sulfurization of Mo Thin Films for High Performance Field-Effect Transistors**

## **3. 1. Introduction**

After the first discovery of graphene, diverse two-dimensional (2D) materials have been explosively developed for various applications. Graphene has been applied to next-generation transparent electrode due to high strength and low sheet resistance,<sup>[1,2]</sup> hexagonal boron nitride (h-BN) have been interested in an excellent insulator,<sup>[3,4]</sup> and transition-metal dichalcogenide (TMDC) have attracted attention in semiconductor field because of band gap property.<sup>[5-18]</sup>

Especially, TMDCs have been paid attention in optical-, electrical device because of their layer dependent tunability, a feature of thin thickness, and intrinsic band gap. Many research groups have shown the change of optical properties depending on the number of layers, including band gap shift,<sup>[9,10]</sup> exciton lifetime, recombination time,<sup>[11-12]</sup> and the change of direct/indirect transition.<sup>[13,14]</sup> Also, it satisfied a qualification as next-generation semiconductor because of their excellent electronic properties.<sup>[5,15-18]</sup>

Among these TMDCs, molybdenum disulfide ( $\text{MoS}_2$ ) has been highlighted, which had mechanical flexibility, thermal stability, high on-off ratio, and high carrier mobility.<sup>[19-26]</sup> Despite its outstanding electrical

performance, its application was restricted by fermi energy pinning, contact resistance with an electrode, related to contact between MoS<sub>2</sub> and metal electrode.<sup>[27-36]</sup> In order to solve these problems, many alternative methods have been proposed; for example, i) the Schottky barrier tuning via work function difference between MoS<sub>2</sub> and contact metal,<sup>[28-32]</sup> ii) contact morphology change from top contact to edge contact, resulting in covalent bonding between the edge atoms of in-plane MoS<sub>2</sub> and metal.<sup>[33-36]</sup> However, the Schottky barrier tuning was limited by the fermi level pinning,<sup>[28-32]</sup> and the edge contact was challenging because of the complex fabrication method.<sup>[33-36]</sup> Although the edge contact was obtained via the phase engineering where the metallic electrode and the semiconductor was obtained by 1T and 2H phase of TMDC based on Mo,<sup>[25,37]</sup> large scale fabrication was still challenging.

Here, we fabricated field-effect transistor (FET) based on MoS<sub>2</sub> by H<sub>2</sub>S treatment of Mo film which was coated by multi-layered (ML) graphene. Mo film was deposited onto SiO<sub>2</sub>/Si substrate by electron-beam (e-beam) evaporation. The ML graphene on the electrode region was adopted as a blocking layer between H<sub>2</sub>S gas and Mo metal, which protected from the reaction between them and preserved intact Mo metal. Therefore, the exposed region of Mo film without the ML graphene was selectively transformed into the MoS<sub>2</sub> channel through a reaction between H<sub>2</sub>S and Mo. Also, the edge contact morphology was observed at the interface between the Mo film with and without ML graphene coating. With ion gel, an electric double-layer

transistor (EDLT) was fabricated and the intact Mo region under 4L graphene was exploited as an electrode of source and drain. Compared with the FET which consisted of MoS<sub>2</sub> channel and Au/Ti electrode, FET with 4L graphene showed better electrical performance, including on-off ratio and electron mobility.

### 3. 2. Experimental

*Graphene synthesis:* Graphene was synthesized under low pressure by chemical vapor deposition on Cu foil at 1000 °C with CH<sub>4</sub> (40 standard cubic centimeter per minute (sccm)) and H<sub>2</sub> (10 sccm) for 30 min. The backside of Cu foil was treated with oxygen plasma (with 100 W for 20 s) to remove the graphene at backside.

*Molybdenum film:* SiO<sub>2</sub> (300 nm)/Si substrate was patterned by using a shadow mask. Molybdenum (Mo) film was deposited on the SiO<sub>2</sub> (300 nm)/Si substrate by e-beam evaporator under 0.1 Å/s of deposition rate at a high vacuum (< 10<sup>-6</sup> torr). Then, through removing the shadow mask after the Mo deposition, the patterned Mo film was fabricated.

*Electrode deposition:* Electrodes were deposited by thermal evaporation at high vacuum. Titanium (Ti) with 10 nm was deposited, followed by deposition of gold (Au) with 50 nm.

*Graphene coating and pattern:* Various stacked graphene was used as a protecting layer from sulfurization during H<sub>2</sub>S treatment. The copper foil was

etched by 80 mM ammonium persulfate (APS) solution and suspended graphene was washed three times in deionized (DI) water. Then, the suspended graphene was transferred onto Mo film. In order to pattern, the graphene on the Mo film was treated by O<sub>2</sub> plasma under 150 W for 35 s with the patterned shadow mask. (O<sub>2</sub> flow rate: 20 sccm)

*Sulfurization:* In order to selectively make the MoS<sub>2</sub> channel, the Mo film which was coated by patterned graphene was treated under mixture of the gases (Ar: 200 sccm, H<sub>2</sub>S: 30 sccm, H<sub>2</sub>: 25 sccm) at 800 °C for 10 min.

*Transmission Electron Microscopy (TEM) observation:* The H<sub>2</sub>S treated Mo film with 4L graphene and the H<sub>2</sub>S treated Mo film was coated by carbon and platinum (Pt). Then, Cross-sectional sample was prepared by focused ion beam milling (FIB). (Helios G4, Thermo Fisher Scientific) Plan view of the H<sub>2</sub>S treated Mo film was prepared by the wet transfer method. The sample was coated by PMMA, followed by etching in buffered oxide etchant (BOE). Both samples were observed by Cs-corrected STEM with Cold FEG. (JEM-ARM200F, JEOL Ltd.)

*Characterization:* Raman spectrum was obtained by inVia Raman Microscope (Renishaw, UK) under 514 nm laser irradiation with 2400 grating. Electrical measurement was implemented by 4200-SCS (Keithley Instruments, USA). XPS data were obtained by K-Alpha X-ray XPS System (Thermo Scientific, USA) with Al K $\alpha$ .



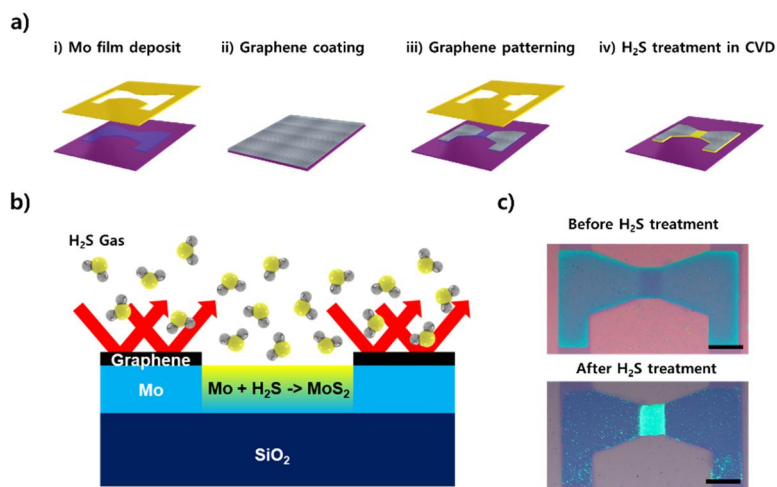


**Figure 3.1.** Scheme of the device fabrication. a) procedure of the FET fabrication. b) schematic image of reaction between Mo film and H<sub>2</sub>S precursor; the Mo film underneath graphene coating was effectively protected from sulfurization reaction, but exposed Mo film, which was not coated by graphene, reacted with H<sub>2</sub>S gas. c) Optical microscope images of the FET device without H<sub>2</sub>S treatment (left) and with H<sub>2</sub>S treatment (right). Scale bar was 100  $\mu$ m.

### 3. 3. Results and Discussion

FET device was fabricated by the sulfurization of Mo film. The Mo film was deposited by e-beam evaporation. (**Figure 3.1a i**) Then, the ML graphene was transferred onto the Mo film. (**Figure 3.1a ii**) In order to form a channel region, the graphene on the Mo film was patterned by reactive ion etching (RIE). (**Figure 3.1a iii**). Although the Mo film with the ML graphene was intact metal, the Mo film without the ML graphene became MoS<sub>2</sub> via the reaction between Mo and H<sub>2</sub>S precursor. (**Figure 3.1a iv** and **Figure 3.1c**)

With various layers of graphene, the ability to protect from sulfurization of the Mo film was confirmed by Raman spectroscopy at diverse reaction conditions. (**Figure 3.5a** and **Figure 3.2**) The E<sub>2g</sub><sup>1</sup> (380 cm<sup>-1</sup>) and A<sub>1g</sub> (406 cm<sup>-1</sup>) mode of MoS<sub>2</sub> were not observed at reaction temperature under 700 °C when various layered graphene was transferred onto the Mo film, while the G and the 2D peak of graphene were changed. (**Figure 3.2** and **3.3**) However, the Raman peaks of MoS<sub>2</sub> was observed when the Mo film with monolayer graphene (1L) was treated by H<sub>2</sub>S gas above 800 °C. (**Figure 3.2a**) Although their intensity of MoS<sub>2</sub> was reduced, they were still observed at reaction temperature over 800 °C when the Mo film was coated by bilayer (2L) graphene. (**Figure 3.2b**) Eventually, in the case of the Mo film with 4 layers (4L) graphene, the characteristic peak of MoS<sub>2</sub> disappeared from 600 °C to 900 °C. (**Figure 3.2c**)

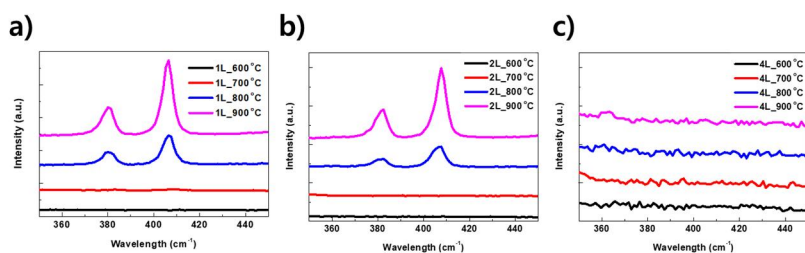


**Figure 3.2.** Raman spectra with the various conditions; XL\_YYY °C where X was the number of graphene layers and YYY was the synthetic temperature of sulfurization. a), b) and c) were Raman spectra of Mo film which was treated H<sub>2</sub>S gas at various temperatures and coated by monolayer, bilayer, and 4 layers of graphene, respectively.

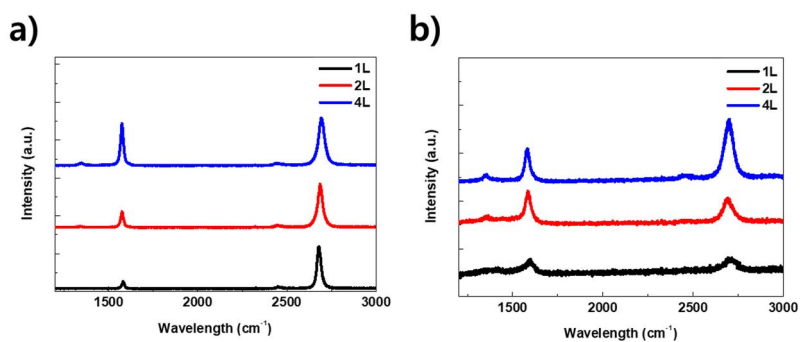


**Figure 3.3.** Raman spectra of graphene. a) Raman spectra of various layered graphene without H<sub>2</sub>S treatment. b) Raman spectra of various layered graphene with H<sub>2</sub>S treatment at 800 °C.

With the increase of reaction temperature, full width at half maximum (FWHM) of  $A_{1g}$  decreased from  $11.3\text{ cm}^{-1}$  ( $600\text{ }^{\circ}\text{C}$ ) to  $6.7\text{ cm}^{-1}$  ( $800\text{ }^{\circ}\text{C}$ ), which was caused by crystallinity of  $\text{MoS}_2$ .<sup>[38]</sup> (**Figure 3.4**) However, over  $800\text{ }^{\circ}\text{C}$ , the FWHM was barely changed ( $6.4\text{ cm}^{-1}$  at  $900\text{ }^{\circ}\text{C}$ ), so that the reaction temperature of  $800\text{ }^{\circ}\text{C}$  was selected.

The  $\text{Mo } 3d_{3/2}$  ( $232.8\text{ eV}$ ),  $\text{Mo } 3d_{5/2}$  ( $229.6\text{ eV}$ ), and  $\text{S } 2s$  ( $226.6\text{ eV}$ ) peaks were well found in X-ray photoelectron spectroscopy (XPS) of bare Mo film and the Mo film with 1L graphene, after  $\text{H}_2\text{S}$  treatment at  $800\text{ }^{\circ}\text{C}$ . The  $\text{S } 2s$  peak in the Mo film with 2L was not found, but the weak intensity of  $\text{S } 2p_{1/2}$  ( $163.6\text{ eV}$ ) and  $\text{S } 2p_{3/2}$  ( $162.4\text{ eV}$ ) was observed.<sup>[39]</sup> These peaks disappeared in the Mo film with 4L graphene. (**Figure 3.5**) Although XPS of Mo was changed when 4L graphene was transferred,  $\text{H}_2\text{S}$  treatment did not affect the binding energy of the Mo film with 4L graphene. (**Figure 3.6**) Therefore, during sulfurization at  $800\text{ }^{\circ}\text{C}$ , the 4L graphene was able to protect from reaction with  $\text{H}_2\text{S}$ .

Based on these results, selective sulfurization was confirmed by Raman mapping when the Mo film was coated by 4L graphene, followed by patterning through  $\text{O}_2$  plasma. (**Figure 3.5c**) The characteristic Raman peak of  $\text{MoS}_2$  was found in the region of the Mo film without 4L graphene, and the 2D peak of graphene from residual graphene was not observed. On the contrary,  $E'_{2g}$  and  $A_{1g}$  of  $\text{MoS}_2$  were not found in the region of the Mo film with 4L graphene.

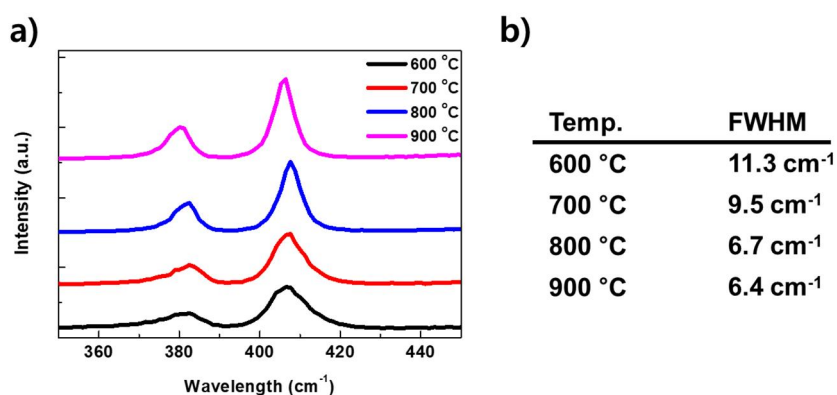


**Figure 3.4.** a) Raman spectra with various reaction temperatures; black line: 600 °C, red line: 700 °C, blue line: 800 °C, magenta line: 900 °C. b) Table of the full half maximum width with various reaction temperatures.

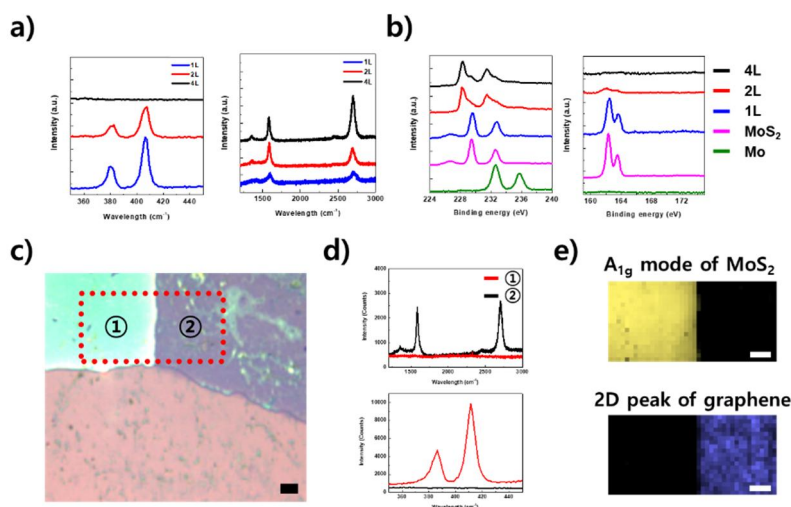


**Figure 3.5.** Characterization of field-effect transistor (FET) based on MoS<sub>2</sub>. a) Raman spectra of Mo film with various layers of graphene coating, after H<sub>2</sub>S treatment. b) XPS spectra of various conditions; 4L, 2L, 1L: 4-, bi-, and mono-layer graphene coating on Mo film with H<sub>2</sub>S treatment, respectively, MoS<sub>2</sub>: Mo film with H<sub>2</sub>S treatment, Mo: bare Mo film. c) Optical microscope image of FET; the red dashed rectangle was concerned with the Raman mapping region. d) Raman spectra of 1 (red line) and 2 (black line) region. e) Raman mapping images; the top and bottom images were formed by using MoS<sub>2</sub> Raman peak (A<sub>1g</sub> mode: 406 cm<sup>-1</sup>) and graphene Raman peak (2D peak: 2700 cm<sup>-1</sup>), respectively. Scale bar was 10 μm.

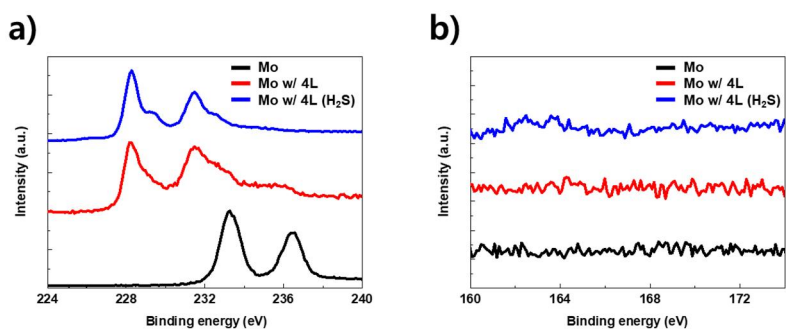


**Figure 3.6.** XPS of Mo film (black), Mo film with 4L graphene (red), H<sub>2</sub>S treated Mo film with 4L graphene. a) Mo binding range. b) sulfur binding range.

These results indicated that selective sulfurization was achieved by patterning of coated the 4L graphene and able to form the channel of MoS<sub>2</sub>. (**Figure 3.5c**)

To further study at the atomic scale, the cross-section of the H<sub>2</sub>S treated Mo film with and without 4L graphene was observed by transmission electron microscopy (TEM). Compared with the 4L graphene-coated Mo film, the thickness of the Mo film without graphene was thicker (with 4L: 6 nm, without 4L: 10nm). (**Figure 3.7a,b**) The image of high-resolution TEM (HR-TEM) revealed it had a layered structure which was composed of 16 layers and its distance between layers was 0.65 nm. (**Figure 3.7b** and **Figure 3.8a**) Also, plan view image of the layer indicated that MoS<sub>2</sub> was composed of small grain (< 200 nm), (**Figure 3.9**) and its d(100) was 0.28 nm which was consistent with MoS<sub>2</sub>.<sup>40</sup> (**Figure 3.7c**) The bulged layered MoS<sub>2</sub> was observed at the interfacial area between the exposed Mo film without 4L graphene and the protected Mo film with 4L graphene. (**Figure 3.7d** and **Figure 3.8b**) The bottom layers of MoS<sub>2</sub> did not connect to the Mo metal, but the top layer of MoS<sub>2</sub> did. As a result, the exposure of H<sub>2</sub>S was able to transform the Mo film into 2D MoS<sub>2</sub> and the reaction was hampered by 4L graphene coating which effectively blocked the contact of H<sub>2</sub>S gas at high temperature. Additionally, the edge contact between MoS<sub>2</sub> and metal electrode was obtained via covalent bonding of them.



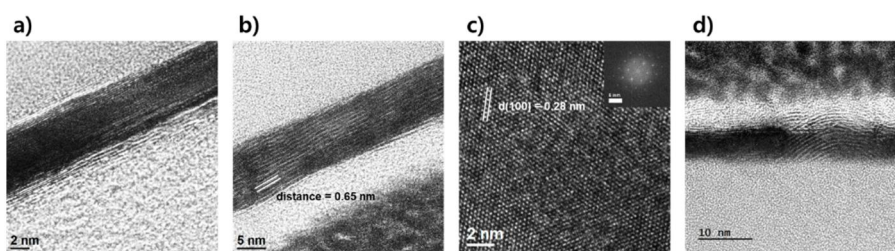


**Figure 3.7.** TEM images of Mo film with and without graphene, after H<sub>2</sub>S treatment. a) graphene coating on Mo film. b) H<sub>2</sub>S exposure region in Mo film without graphene. c) plan view image of the b) region. Inset: FFT pattern of the c). d) The interface between the exposed Mo region (without 4L graphene) and the protected Mo region with 4L graphene, after H<sub>2</sub>S treatment

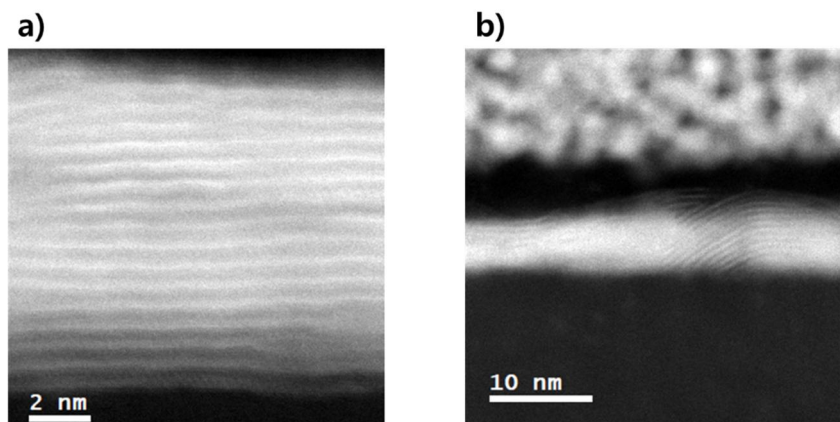


**Figure 3.8.** STEM images of a) the H<sub>2</sub>S treated Mo film and b) interface between the Mo film with and without 4L graphene.

The EDLT had a benefit, including fermi energy tuning, reducing trapping states, and a thin dielectric layer which was formed at the interface between semiconductor and ion gel when gate voltage was applied.<sup>[21,41,42]</sup> Therefore, we fabricated the FET based MoS<sub>2</sub> with ionic liquid of DEME-TFSI (N,N-diethyl-N-methyl-N-(2-methoxyethyl) ammonium bis (trifluoromethyl-sulfonyl) imide) which was widely employed as ionic liquid in FET based on MoS<sub>2</sub>.<sup>[21,41-43]</sup> **(Figure 3.11)** In case of the MoS<sub>2</sub> with 4L graphene coating (MoS<sub>2</sub>-4L), the intact Mo film region was employed as electrode of source and drain, which maintained its metallic property. **(Figure 3.10a)** However, in the case of the MoS<sub>2</sub>, the electrode of source and drain was formed by deposition of Au/Ti (50 nm/ 10nm) (MoS<sub>2</sub>-Au) due to the absence of the electrode. **(Figure 3.10b)**

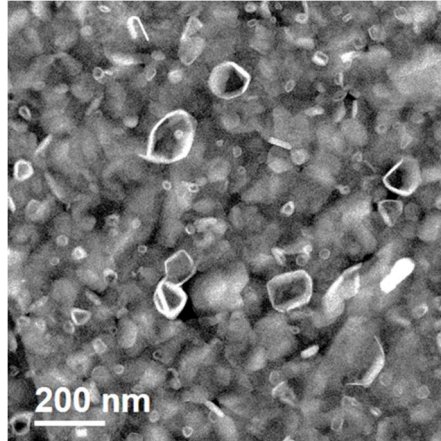


**Figure 3.9.** STEM images of plan view of MoS<sub>2</sub>.

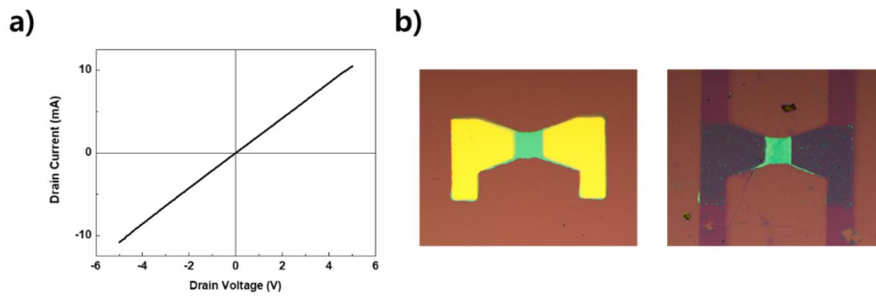


**Figure 3.10.** a) I-V curve ( $I_{DS}$  vs.  $V_{DS}$ ) of the electrode region of MoS<sub>2</sub>-4L. b) Optical images of FETs; left = MoS<sub>2</sub>-Au, right = MoS<sub>2</sub>-4L.

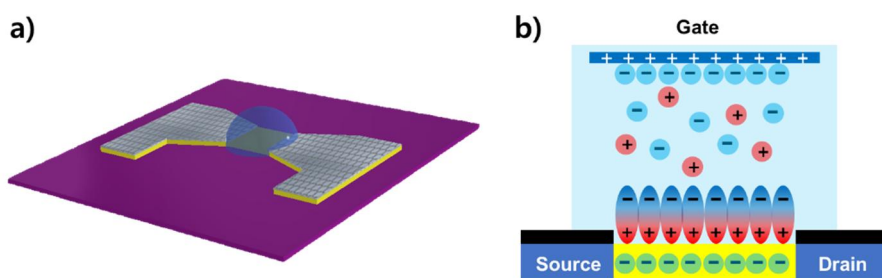


**Figure 3.11.** a) A schematic image of the EDLT based 4L graphene-coated MoS<sub>2</sub> with ion gel. b) a schematic image of the EDLT during operating; when the gate voltage was applied, charged ion in ion gel was oriented by electrical gradient, and the electrical double layer was formed at the interface between MoS<sub>2</sub> and ion gel, which was a great dielectric layer.

Compared with MoS<sub>2</sub>-Au, the electrical properties of MoS<sub>2</sub>-4L was implemented under various condition. In order to calculate electron mobility, the threshold voltage ( $V_{th}$ ) was extracted at the linear range in the transfer curve of the decimal scale. (MoS<sub>2</sub>-4L  $V_{th}$ : 3.88 V, MoS<sub>2</sub>-Au  $V_{th}$ : 3.71 V) (**Figure 3.12a**) Drain current was represented by the equation (1):

$$I_D = \mu C \frac{W}{L} \{ (V_G - V_{th}) V_{DS} - \frac{1}{2} V_{DS}^2 \} \quad (1),$$

where  $I_D$  was drain current,  $\mu$  was electron mobility,  $V_G$  was the applied voltage at the gate,  $C$  was capacitance,  $W$  was channel width, and  $L$  was channel length. With  $7.2 \mu\text{F}/\text{cm}^2$  as the capacitance for electron,<sup>[41,42]</sup> the calculated electron mobility of MoS<sub>2</sub>-4L and MoS<sub>2</sub>-Au was  $21.78 \text{ cm}^2/(\text{V}\cdot\text{s})$  and  $2.87 \text{ cm}^2/(\text{V}\cdot\text{s})$ , respectively. (**Figure 3.12b**) Also, the On-off ratio of MoS<sub>2</sub>-4L and MoS<sub>2</sub>-Au were  $\sim 10^3$ ,  $\sim 10^2$ , respectively, and the output curve of them was carried out with various gate voltage. (**Figure 3.12c,d**) As a result, MoS<sub>2</sub>-4L exhibited better electrical properties, indicating that the contact geometry might affect the performance of the device.

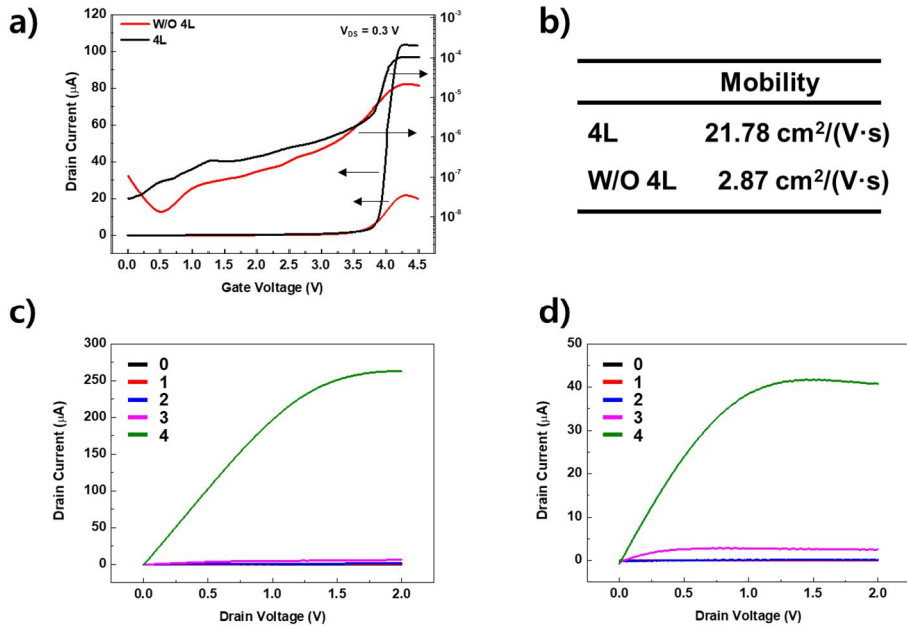


**Figure 3.12.** Electrical properties of FET based on MoS<sub>2</sub>. a) Transfer curve ( $I_D$  vs.  $V_G$ ); the black line = MoS<sub>2</sub>-4L, the red line = MoS<sub>2</sub>-Au. b) mobility of electron.  $V_{th}$  was extracted by linear fitting at the transfer curve of the decimal scale, followed by the extraction of the intercept value of the x-axis.  $V_{th}$  of MoS<sub>2</sub>-4L and MoS<sub>2</sub>-Au was 3.88 V and 3.71 V, respectively. The capacitance of ion gel was 7.2  $\mu$ F for electrons. c) output curve of MoS<sub>2</sub>-4L with various conditions (from  $V_G = 0$  V to  $V_G$  4.5 V). d) output curve of MoS<sub>2</sub>-4L with various conditions (from  $V_G = 0$  V to  $V_G$  4.5 V. Channel width and length of both of devices were 100  $\mu$ m and 80  $\mu$ m, respectively.

### 3. 4. Conclusion

In conclusion, we fabricate FET based on MoS<sub>2</sub> by the combined method which consisted of Mo deposition, graphene coating, and H<sub>2</sub>S treatment. The regions of the electrode and channel were simply formed, corresponding to the ML graphene coating. After H<sub>2</sub>S treatment, the Mo film without 4L graphene was transformed into the ML layered MoS<sub>2</sub>, but the Mo film with 4L graphene was intact. The characteristic MoS<sub>2</sub> signals of Raman spectroscopy and XPS were only detected at the channel region where the Mo film was exposed by the H<sub>2</sub>S precursor. Although the bulged MoS<sub>2</sub> was observed at the interface between the channel and the electrode, the connection of them was found and indicated that the geometry of the contact was the edge contact by which covalent bonding between MoS<sub>2</sub> and Mo, corresponding to the channel and the electrode, was formed. The intact region of the Mo film under 4L graphene was exploited as the source and drain electrode due to its metallic property. The on-off ratio and electron mobility of MoS<sub>2</sub>-4L were 10 times higher than that of MoS<sub>2</sub>-Au. Although MoS<sub>2</sub>-4L had a small grain that caused frequent electron scattering and current leakage, the electrical performance was able to be improved by the change of contact geometry from simple graphene coating. Therefore, this device will be able to enhance the electrical performance through MoS<sub>2</sub> grain size control and optimization of the layer number of MoS<sub>2</sub>. Finally, graphene coating and in situ sulfurization will be widely used as the simple method of edge contact formation in FET based on two-dimensional layered material.

### 3. 5. References

- [1] S. Bae; H. Kim; Y. Lee; X. Xu; J.-S. Park; Y. Zheng; J. Balakrishnan; T. Lei; H. R. Kim; Y. I. Song; Y.-J. Kim; K. S. Kim; B. Özyilmaz; J.-H. Ahn; B. H. Hong; S. Lijima. *Nat. Nanotechnol.* **2010**, *5*, 574-578
- [2] J. Ryu; Y. Kim; D. Won; N. Kim; J. Park; E.-K. Lee; D. Cho; S.-P. Cho; S. J. Kim; G. H. Ryu; H.-A-S. Shin; Z. Lee; B. H. Hong; S. Cho. *ACS Nano* **2014**, *8*, 950-956
- [3] X. Wu; R. Ge; P.-A. Chen; H. Chou; Z. Zhang; Y. Zhang; S. Banerjee; M.-H. Chiang; J. C. Lee; D. Akinwande. *Adv. Mater.* **2019**, *31*, 1806790
- [4] K. S. Novoselov; A. Mishchenko; A. Carvalho; A. H. C. Neto. *Science* **2016**, *353*, 461
- [5] W. Huang; L. Gan; H. Yang; N. Zhou; R. Wang; W. Wu; H. Li; Y. Ma; H. Zeng; T. Zhai. *Adv. Funct. Mater.* **2017**, *27*, 1702448
- [6] Z. Cai; B. Liu; X. Zou; H.-M. Cheng. *Chem. Rev.* **2018**, *118*, 6091-6133
- [7] D. Wu; T. Min; J. Zhou; C. Li; G. Ma; G. Lu; M. Xia; Z. Gu. *Sci. Rep.* **2017**, *7*, 15166
- [8] J. Liu; M. Zheng; L. Wang; Y. Chen; Z. Xing; T. Zhang; Z. Liu; J. Zuo; F. Nan; R. G. Mendes; S. Chen; F. Ren; Q. Wang; M. H. Rümmeli; L. Fu. *Small* **2016**, *12*, 5741-5749
- [9] Z. Yang; W. Jie; C.-H. Mak; S. Lin; H. Lin; X. Yang; F. Yan; S. P. Lau; J. Hao. *ACS Nano* **2017**, *11*, 4225-4236
- [10] D. A. Bandurin; A. V. Tyurnina; G. L. Yu; A. Mishchenko; V. Zólyomi; S.



- V. Morozov; R. K. Kumar; R. V. Gorbachev; Z. R. Kudrynskyi; S. Pezzini;  
Z. D. Kovalyuk; U. Zeitler; K. S. Novoselov; A. Pantanè, L. Eaves; I. V.  
Grigorieva; V. I. Fal'Ko; A. K. Geim; Y. Cao. *Nat. Nanotechnol.* **2017**, *12*,  
223
- [11] D. Unichek; A. Ciarrocchi; A. Avsar; Z. Sun; K. Watanabe; T. Taniguchi;  
A. Kis. *Nat. Nanotechnol.* **2019**, *14*, 1104-1109
- [12] L. A. Jauregui; A. Y. Joe; K. Pistunova; D. S. Wild; A. A. High; Y. Zhou;  
G. Scuri; K. D. Greve; A. Sushko; C.-H. Yu; T. Taniguchi; K. Watanabe; D.  
J. Needleman; M. D. Lukin; H. Park; P. Kim. *Science* **2019**, *366*, 870-875
- [13] G. W. Mudd; M. R. Molas; X. Chen; V. Zólyomi; K. Nogajewski; Z. R.  
Kudrynskyi; Z. D. Kovalyuk; G. Yusa; O. Makarovsky; L. Eaves; M.  
Potemski; V. I. Fal'ko; A. Pantanè. *Sci. Rep.* **2016**, *6*, 39619
- [14] I. Tanabe; M. Gomez; W. C. Coley; D. Le; E. M. Echeverria; G. Stecklein;  
V. Kandyba; S. K. Balijepalli; V. Klee; A. E. Nguyen; E. Preciado; I-H. Lu;  
S. Bobek; D. Barroso; D. Martinez-Ta; A. Barinov; T. S. Rahman; P. A.  
Dowben; P. A. Crowell; L. Bartels. *Appl. Phys. Lett.* **2016**, *108*, 252103
- [15] H.-L. Tang; M.-H. Chiu; C.-C. Tseng; S.-H. Yang; K.-J. Hou; S.-Y. Wei;  
J.-K. Huang; Y.-F. Lin; C.-H. Lien; L.-J. Li. *ACS Nano* **2017**, *11*, 12817-  
12823
- [16] J.-B. Lee; Y. R. Lim; A. K. Katiyar, W. Song; J. Lim; S. Bae; T.-W. Kim;  
S.-K. Lee; J.-H. Ahn. *Adv. Mater.* **2019**, *31*, 1904194
- [17] M. Li; C.-Y. Lin; S.-H. Yang; Y.-M. Chang; J.-K. Chang; F.-S. Yang; C.

- Zhong; W.-B. Jian; C.-H. Lien; C.-H. Ho; H.-J. Liu; R. Huang; W. Li; Y.-F. Lin; J. Chu. *Adv. Mater.* **2018**, *30*, 1803690
- [18] Y. Gong; S. Lei; G. Ye; B. Li; Y. He; K. Keyshar; X. Zhang; Q. Wang; J. Lou; X. Liu; R. Vajtai; W. Zhou; P. M. Ajayan. *Nano Lett.* **2015**, *15*, 6135-6141
- [19] H. Liu; A. T. Neal; P. D. Ye. *ACS Nano* **2012**, *6*, 8563-8569
- [20] X. Zou; J. Wang; C.-H. Chiu; Y. Wu; X. Xiao; C. Jiang; W.-W. Wei; L. Mai; T. Chen; J. Li; J. C. Ho; L. Liao. *Adv. Mater.* **2014**, *26*, 6255-6261
- [21] Y. Zhang; J. Ye; Y. Matsushashi; Y. Iwasa. *Nano Lett.* **2012**, *12*, 1136-1140
- [22] L. Yu; Y.-H. Lee; X. Ling; E. J. G. Santos; Y. C. Shin; Y. Lin; M. Dubey; E. Kaxiras; J. Kong; H. Wang; T. Palacios. *Nano Lett.* **2014**, *14*, 3055-3063
- [23] Y. Lee; J. Lee; H. Bark; I.-K. Oh; G. H. Ryu; Z. Lee; H. Kim; J. H. Cho; J.-H. Ahn; C. Lee. *Nanoscale* **2014**, *6*, 2821
- [24] J. Kwon; J.-Y. Lee; Y.-J. Yu; C.-H. Lee; X. Cui; J. Hone; G.-H. Lee. *Nanoscale* **2017**, *9*, 6151
- [25] R. Kappera; D. Voiry; S. E. Yalcin; B. Branch; G. Gupta; A. D. Mohite; M. Chhowalla. *Nat. Mater.* **2014**, *13*, 1128
- [26] X. Cui; G.-H. Lee; Y. D. Kim; G. Arefe; P. Y. Huang; C.-H. Lee; D. A. Chenet; X. Zhang; L. Wang; F. Ye; F. Pizzocchero; B. Jessen; K. Watanabe; T. Taniguchi; D. A. Muller; T. Low; P. Kim; J. Hone. *Nat. Nanotechnol.* **2015**, *10*, 534
- [27] A. Allain; J. Kang; K. Banerjee; A. Kis. *Nat. Mater.* **2015**, *14*, 1195

- [28] S. Das; H.-Y. Chen; A. V. Pernumatcha; J. Appenzeller. *Nano Lett.* **2013**, *13*, 100-105
- [29] G.-S. Kim; S.-H. Kim; J. Park; K.-H. Han; J. Kim; H.-Y. Yu. *ACS Nano* **2018**, *12*, 6292-6300
- [30] S. Chuang; C. Battaglia; A. Azcatl; S. McDonnell; J. S. Kang; X. Yin; M. Tosun; R. Kapadia; H. Fang; R. M. Wallace; A. Javey. *Nano Lett.* **2014**, *14*, 1337-1342
- [31] W. Liu; D. Sarkar; J. Kang; W. Cao; K. Banerjee. *ACS Nano* **2015**, *9*, 7904-7912
- [32] S.-S. Chee; D. Seo; H. Kim; H. Jang; S. Lee; S. P. Moon; K. H. Lee; S. W. Kim; H. Choi; M.-H. Ham. *Adv. Mater.* **2019**, *31*, 1804422
- [33] A. Jain; Á. Szabó; M. Parzefall; E. Bonvin; T. Taniguchi; K. Watanabe; P. Bharadwaj; M. Luisier; L. Novotny. *Nano Lett.* **2019**, *19*, 6914-6923
- [34] H. Choi; B. H. Moon; J. H. Kim; S. J. Yun; G. H. Han; S. Lee; H. Z. Gul; Y. H. Lee. *ACS Nano* **2019**, *13*, 13169-13175
- [35] Z. Cheng; Y. Yu; S. Singh; K. Price; S. G. Noyce; Y.-C. Lin; L. Cao; A. D. Franklin. *Nano Lett.* **2019**, *19*, 5077-5085
- [36] Z. Yang; C. Kim; K. Y. Lee; M. Lee; S. Appalakondaiah; C.-H. Ra; K. Watanabe; T. Taniguchi; K. Cho; E. Hwang; J. Hone; W. J. Yoo. *Adv. Mater.* **2019**, *31*, 1808231
- [37] J. H. Sung; H. Heo; S. Si; Y. H. Kim; H. R. Noh; K. Song; J. Kim; C.-S. Lee; S.-Y. Seo; D.-H. Kim; H. K. Kim; H. W. Yeom; T.-H. Kim; S.-Y. Choi;

- J. S. Kim; M.-H. Jo. *Nat. Nanotechnol.* **2017**, *12*, 1064
- [38] X. Xu; G. Das; X. He; M. N. Hedhili; E. D. Fabrizio; X. Zhang; H. N. Alshareef. *Adv. Funct. Mater.* **2019**, *29*, 1901070
- [39] Q. D. Truong; M. K. Devaraju; Y. Nakayasu; N. Tamura; Y. Sasaki; T. Tomai; I. Honma. *ACS Omega* **2017**, *2*, 2360-2367
- [40] Z. Du; S. Yang; S. Li; J. Lou; S. Zhang; S. Wang; B. Li; Y. Gong; L. Song; X. Zou; P. M. Ajayan. *Nature* **2020**, *577*, 492
- [41] J. Pu; Y. Yomogida; K.-K. Liu; L.-J. Li; Y. Iwasa; T. Takenobu. *Nano Lett.* **2012**, *12*, 4013-4017
- [42] Y. J. Zhang; J. T. Ye; Y. Yomogida; T. Takenobu; Y. Iwasa. *Nano Lett.* **2013**, *13*, 3023-3028
- [43] G. Gao; J. Yu; X. Yang; Y. Pang; J. Zhao; C. Pan; Q. Sun; Z. L. Wang. *Adv. Mater.* **2019**, *31*, 1806905

## Chapter 4. Conclusion

In this thesis, the application of 0D nanoparticles and 2D semiconductors for drug delivery and transistor applications are described, respectively.

In Chapter 2, we discussed the biomedical applications of the nanoparticles loaded with drug molecules. It was confirmed that various-sized nanoparticles with different porosity can be synthesized by applying the growth principle of thin-film technology. Depending on the surface energy, the growth mechanism shows FM growth (core-shell), VW growth (island), and SK growth (FM + VW) growth. The dual pore system was developed to achieve a combinational anti-cancer effect, and it was confirmed that the nanoparticles can be loaded with nucleic acids and anticancer substances (siRNA and doxorubicin) simultaneously for better stability during delivery *in vivo*. The loaded materials were effectively transported into cancer cells, and the drug molecules were released to show the superior anticancer effect.

Chapter 3 describes the synthesis and application of 2D molybdenum disulfide ( $\text{MoS}_2$ ) thin films for FETs with a gradient composition that can minimize the contact resistance. First, thin layers of Mo was deposited by thermal evaporation, followed by selective masking of the electrode areas with graphene as a gas-impermeable layer. Thereafter, the unmasked channel region was sulfurized by hydrogen sulfide ( $\text{H}_2\text{S}$ ) gas. As a result, only the exposed Mo surface was selectively transformed to  $\text{MoS}_2$ , where the gradient of chemical composition from Mo to  $\text{MoS}_2$  is formed at the interface. It was

found that such gradual contact enables the smooth and successive change of work functions, lowered Schottky barriers, increased on-off ratio and charge carrier mobility. The encapsulation performance depends on the number of graphene layers, and 4-layer graphene shows almost perfect encapsulation of Mo electrodes against sulfurization gas.

In conclusion, we proposed the 0D dual pore nanoparticles systems as an efficient 2-way drug delivery system for anticancer therapy. In addition, the gradient contact between Mo electrodes and MoS<sub>2</sub> channel is proposed to maximize the electrical performance of FETs. As seen in the above studies, engineering the structures and properties of 0~2D nanomaterials is extremely important to achieve novel functions or higher performance for more practical applications. Further studies are required to better understand the growth mechanism and their physical and chemical properties, which is crucial to expand it to various biomedical, display, semiconductor, and energy applications

## 요 약 (국문초록)

최근 나노 기술은 근래 들어 급격하게 발전하고 있으며, 전 산업 분야에 응용이 되고 있다. 또한 나노 크기에서만 관찰 가능한 현상들은 많은 과학자들의 연구 대상이 되어지고 있다. 나노 입자는 입자의 크기가 나노로 작아짐에 따른 현상들을 뚜렷하게 관찰할 수 있기 때문에, 수많은 과학자들이 이에 관련된 연구를 진행해왔다. 입자 크기에 따른 발광 에너지 변화는 대표적으로 나노 크기 입자에서 발견되는 현상이며, 이외에도 초상자성 특성, 촉매 특성의 강화는 나노 크기 입자에서 자주 발견되는 특징들이다. 최근 들어서는 나노 입자를 이용한 디스플레이가 산업적으로 주목받고 있으며, 리튬 이온 전지에 쓰이는 양극제는 나노 입자의 산업적 응용의 또 다른 예시이다.

이러한 나노 입자 이외에도 우리 주변에서 나노 기술이 접목된 예시들은 쉽게 찾아볼 수 있다. 핸드폰에 사용되는 반도체나 수 많은 부품들은 그 예시들이며, 나노 기술로 인하여 전자 기기들의 소형화가 더욱 가속화될 수 있었다. 반도체 공정에 사용되는 박막 기술은 산업에 사용되는 주요 기술 중 하나이며, 제품의 수율과 질에 바로 직결되는 기술이기 때문에 그에 관련된 많은 연구가 이루어져 왔다. 나노 입자와 마찬가지로, 박막에서도 그 두께가 나노 크기가 될 때 특이한 현상들이 관찰된다.

그래핀으로 대변되는 2 차원 물질은 원자 수준 두께를 갖는 초 박막 물질로, 처음 발견이 된 이후 여러 우수한 특성들로 인해 꿈의

물질로 불러왔다. 이러한 성질들을 이용하여 투명전극, 반도체 등 여러 산업에 이 물질을 응용, 대체하려는 연구가 활발하게 진행되고 있다. 또한, 2 차원 물질들은 위상학적 효과, 전자의 스핀 홀 효과, 초전도현상 등 기존 박막 물질에서 관찰하기 힘든 많은 현상들을 관찰할 수 있어서 많은 과학자들이 주목을 하고 있다.

최근, 나노 기술은 의생명공학쪽으로 많이 유입이 되고 있다. 나노 입자를 이용한 약물전달과 조영제 연구가 대표적인 사례들이고, 이를 이용한 임상시험들이 활발하게 진행되고 있다. 이외에도 전자기기들을 이용한 진단 도구, 웨어러블 장치를 이용한 스마트 헬스케어 등, 나노 기술과 의생명 기술 융합의 수 많은 예시들을 쉽게 찾아볼 수 있다.

본 논문에서는 나노 기술에 대한 전반적인 설명과 더불어, 나노 기술의 여러 분야의 응용에 대해 기술을 하고자 한다. 1 장에서는 나노 기술의 이론적 배경과 응용에 관한 내용을 기술하였으며, 2 장에서는 약물 적재가 된 나노 입자를 이용한 의생명공학적 활용에 관한 결과를 기술하였다. 사용된 나노 입자는 기존 박막 기술에서 활용되는 성장 원리를 적용시켜 합성하였고, 이 입자에 헥산과 향암 물질을 적재하였다. 적재된 물질들은 나노 입자로 인하여 효과적으로 암세포 내로 운반이 되며, 이로 인해 더 뛰어난 향암 효과를 나타냈다.

3 장에서는 2 차원 물질을 이용하여 트랜지스터를 제작한 뒤 물리적, 전기적 특성을 측정한 결과에 대하여 기술하였다. 2 차원 물질은



화학증착기상법을 통해 몰리브데늄 다이설파이드 ( $\text{MoS}_2$ ) 기판으로 제작되었으며, 다층 그래핀으로 몰리브데늄 박막을 코팅한 뒤, 패터닝을 통해 다층 그래핀의 원하는 부위를 식각하였다. 이 후, 황화수소 ( $\text{H}_2\text{S}$ ) 기체를 이용하여, 노출된 금속 표면만 선택적으로 황화반응을 유도하여 반도체의 채널을 형성시켰다. 생성된 반도체는 가장자리 접촉 형태를 갖게 되며, 이로 인해 우수한 전기적 특성을 나타냈다.

마지막 4 장에서는 위 실험들에 관한 결론을 기술하는 것으로 이 논문을 마무리하였다.

주요어 : 나노 기술, 나노 입자, 2 차원 물질, 항암 효과,

화학증착기상법, 트랜지스터

학 번 : 2015-30978

이 중 환